ELSEVIER

Contents lists available at ScienceDirect

Ocean Engineering

journal homepage: www.elsevier.com/locate/oceaneng





Localization and topological observability analysis of a moored floating structure using mooring line tension measurements

Zhengru Ren ^a, Hongyu Zhou ^b, Binbin Li ^a, Zhenzhong Hu ^a, Menghong Yu ^c, Wei Shi ^{d,*}

- a Institute for Ocean Engineering, Shenzhen International Graduate School, Tsinghua University, Shenzhen, 518071, China
- b Department of Aerospace Engineering, University of Michigan, Ann Arbor, MI 48109-2140, United States of America
- ^c Institute of Automation, Jiangsu University of Science and Technology, Zhenjiang, 212003, China
- d Deepwater Engineering Research Centre, State Key Laboratory of Coastal and Offshore Engineering, Dalian University of Technology, Dalian 116024, China

ARTICLE INFO

Keywords: Mooring structures Position mooring Position reference Simultaneous localization and mapping

ABSTRACT

Mooring is a widely used stationkeeping approach for floating structures. The main contribution of this paper is to propose a novel localization scheme, which provides additional real-time position references and estimates the unknown anchor positions to a moored structure simultaneously using tension measurements from the mooring monitoring system. The proposed method enhances the safety of moored floating structures by extracting redundant position information from tension measurements instead of using satellite signals. A line-of-sight model that transforms tension measurements into range signals is developed. Fairleads, turret dynamics, and slow-varying current profiles are considered to provide a more realistic and robust tension-based localization scheme than early research. A distance-only sensor network is constructed, and graph rigidity theory is applied to analyze its topological observability. Two simplified models are presented for some specific applications: (1) to find the broken anchors offline with stored data for any vessels equipped with tension cells and (2) to position the moored structures with known anchor positions. Sensitivity studies show that the influence of unknown surface current is small, while the effects of unknown current profiles are larger. The positioning accuracy can be improved by increasing the number of virtual vessels.

1. Introduction

Mooring is a widely used stationkeeping approach to constrain the position of floating structures in water (Ja'e et al., 2022). It applies to both permanent and temporary operations. Several state-of-the-art industrial innovations have motivated increasing attention for mooring systems, i.e., floating bridge (Dai et al., 2021; Peng et al., 2021), floating wind turbines (Campanile et al., 2018; Shi et al., 2023; Zeng et al., 2022; Zhang et al., 2022), floating fish farms (Li et al., 2019), thruster-assisted position mooring systems (Zhen et al., 2018; Zhou et al., 2018), etc.

It has been reported that the main class societies experience one anchor lost per 100 ships each year (Nord, 2011). The risk of losing anchors and chains is high for a service life of more than 20 years. Broken chains and anchors are considered wrecks and according to the IMO convention, ship owners are responsible for the costly wreck removal (Ratcovich, 2008). Therefore, techniques that can quickly locate and remove the lost anchors after mooring failures are promising.

Commercial mooring line tension monitoring systems have become available, resulting in their availability for tension measurement. A

winch load monitoring system not only enhances the systematic autonomy but also detects fatigue and line breakage (May et al., 2008; Lee et al., 2021). A robust dynamic mooring tension control scheme is theoretically addressed in Aamo and Fossen (1999). An experimental verification is conducted by Nguyen et al. (2011) and Ji et al. (2015).

Collaborative position location is a localization technique. In the localization technique framework, nodes in a sensor network can collaboratively determine their locations. These techniques can be classified into deterministic and probabilistic methods. Approaches based on maximum likelihood, such as second-order cone programming (SOCP) and semidefinite programming (SDP), are widely applied deterministic optimization-based approaches (Lui et al., 2009; Naddafzadeh-Shirazi et al., 2014; Deng et al., 2022). SOCP is much faster than SDP due to lower computational complexity, while SDP has a higher localization accuracy (Tseng, 2007). However, these one-shot methods are not sufficiently robust, since it is impossible to apply them to the algorithm with uncertain landmarks. An additional challenge is that the system is not a closed-loop system, which makes the model unlikely to ensure stability.

E-mail addresses: zhengru.ren@sz.tsinghua.edu.cn (Z. Ren), zhouhy@umich.edu (H. Zhou), libinbin@sz.tsinghua.edu.cn (B. Li), hu.zhenzhong@sz.tsinghua.edu.cn (Z. Hu), ymhzj2691@163.com (M. Yu), weishi@dlut.edu.cn (W. Shi).

^{*} Corresponding author.

Simultaneous localization and mapping (SLAM) is a technique applied in robotics to locate the robot with uncertain landmarks and no access to posref through a joint estimation of pose and landmarks (Gustafsson, 2010). Normally, an extended Kalman filter (EKF), particle filter, and FastSLAM are the most popular approaches for SLAM (Durrant-Whyte and Bailey, 2006; Ren et al., 2019).

To design an observer for a distance-only localization problem, observability is the first factor to be considered. For a steady network, the number of nodes with known positions should be at least 3 in two-dimensional (2D) plane and 4 in three-dimensional space. However, the number of nodes with known positions can be reduced by for a dynamic network, which is contributed by the motion of the nodes. For example, the observability of popular single-beacon navigation for autonomous underwater vehicles is discussed in Arrichiello et al. (2013). In formation control of multiple robots, rigidity graph theory is applied to evaluate the topological stability.

The idea of localization for a thruster-assisted position mooring (TAPM) system using real-time tension measurements is firstly proposed in Ren et al. (2015) with known anchor positions in a current-free environment. Then, the study is preliminarily extended to a scenario with unknown anchors (Ren and Skjetne, 2016b). However, systematic observability analysis lacks and the verification is limited. In this paper, we further extend the tension-based localization scheme to a more general scenario, i.e., anchor positions are unknown, and mooring lines are exposed to depth-dependent time-varying current profiles. The motion estimates can also be applied to predict the vessel motions in tens of seconds, for example, by sparse regression (Ren et al., 2023) and neural networks (Guo et al., 2022). The topology of the sensor network is verified with systematic analysis. An EKF-based SLAM technique is adopted to locate the vessel with tension measurements. An additional simplified model is applicable to track uncertain anchor positions for any vessels equipped with tension cells. As a result, the costs to remove the lost anchors will be reduced.

This paper is organized as follows. In Section 2, the mathematical modeling of a moored vessel, mooring line, and turret dynamics are reviewed. In Section 3, the possibility of generating a range (or distance) measurement from a real-time tension measurement is investigated. Assumptions are made to transform the tension measurement into a range signal. The influence of the tension noise, current-induced loads, and dynamic tension aroused from wave-induced vessel motion are discussed. A sensor network is constructed, and the problem is formulated. Topological observability is analyzed in Section 4. The state-space model and the EKF-SLAM algorithm are proposed in Section 5. Simulation results of sensitivity studies are illustrated in Section 6. Section 7 concludes the paper.

Notations: $1_{m\times n}$ and $0_{m\times n}$ denote $m\times n$ matrices with all elements equal to 1 and 0, respectively. Specially, 1_m and 0_m are vector with n=1. Identity matrix with a size $m\times m$ is denoted by I_m . $|\cdot|$ denotes the standard Euclidean norm. The eigenvalues of a matrix $A\in\mathbb{R}^{n\times n}$ is denoted by $\lambda_i(A)$. After sorting, with increasing values, $\lambda_1(A)\leq \lambda_2(A)\leq \cdots \leq \lambda_n(A)$, and $\lambda_{\min}=\lambda_1$, $\lambda_{\max}=\lambda_n$. The frequently used symbols and their denotations are summarized in Table 5.

In localization, an anchor node denotes the node with the known position in a network. To avoid confusion with a physical anchor, we use a beacon hereafter.

Lemma 1 (Weyl's Inequality). Let A and B be $n \times n$ Hermitian matrices, with their respective eigenvalues ordered as $\lambda_1(\cdot) \leq \lambda_2(\cdot) \leq \cdots \leq \lambda_n(\cdot)$. The following inequalities hold

$$\lambda_{i+i-1}(A+B) \ge \lambda_i(A) + \lambda_i(B),\tag{1a}$$

$$\lambda_{i+i-n}(A+B) \le \lambda_i(A) + \lambda_i(B). \tag{1b}$$

2. System modeling

The system configuration is presented in Fig. 1. A floating structure is spreadly moored by m mooring lines, exposed to wind, waves, and current. The bottoms of the mooring lines are fixed on the seafloor by anchors. Each mooring line is connected to the turret through its corresponding fairlead. The turret rotates about a vertical axis at the center of turret (COT) by the total torque induced by the mooring lines. The vessel is weathervaning, its horizontal position is constrained by the mooring system, and its heading remains against the main wave direction

Three right-handed inertial coordinate systems are adopted in this paper.

- North-east-down (NED) reference frame {N}: The origin is located at the equilibrium point on the free water surface, where the vessel stays constantly without any environmental loads and thruster inputs. The x-, y-, and z-axes are northward, eastward, and downward, respectively.
- Body-fixed reference frame {B}: The origin is at the COT of the vessel with x^b-, y^b-, and z^b-axes pointing to the stem, starboard, and downward, respectively.
- Anchor_i-fixed reference frame $\{A_i\}$: The origin O_{Ai} is placed at the ith anchor on the seafloor. The x^{a_i} -axis directs to the projection of the ith fairlead on the seafloor, and the z^{a_i} -axis points downwards.

Reference frames $\{N\}$ and $\{B\}$ are mainly used in deduction and simulation. Reference frames $\{A_i\}$ are only used to initialize the mooring lines. The motion of a floating vessel can be superposed by the low-frequency (LF) model and the wave-frequency (WF) model. The stationkeeping model of a position mooring system has been intensively reviewed (Skjetne and Ren, 2020).

2.1. Low-frequency model

The LF model is caused by the slow-varying second-order wave drift force, current loads, and mean-wind loads. The LF stationkeeping model (Fossen, 2011; Wu, 2022) is given by

$$\dot{\eta} = R(\psi)\nu,\tag{2a}$$

$$\dot{b} = -T_b^{-1}b + E_b w_b, {2b}$$

$$M\dot{v} = -Dv + R^{\mathsf{T}}(\psi)b + \tau_m + \tau_c, \tag{2c}$$

where $\eta = [x,y,\psi]^{\top}$ consists of LF position and heading orientation of the vessel relative to $\{N\}$, $v = [u,v,r]^{\top}$ represents the corresponding translational and rotational velocities decomposed in a vessel-fixed reference, $R(\psi) \in \mathbb{R}^{3\times 3}$ denotes the transformation matrix from $\{B\}$ to $\{N\}$, $E_b \in \mathbb{R}^{3\times 3}$ is a diagonal scaling matrix, $M \in \mathbb{R}^{3\times 3}$ is the generalized system inertia matrix including zero-frequency added mass components, $D \in \mathbb{R}^{3\times 3}$ denotes the linear damping matrix, $b \in \mathbb{R}^3$ is a slowly varying bias vector, $\tau_c \in \mathbb{R}^3$ represents the thruster input vector, and $\tau_m \in \mathbb{R}^3$ is the mooring load vector.

2.2. Wave-frequency model

Resulting from the first-order wave loads, the state-space form of the WF model is given by

$$\dot{\xi} = A_w \xi + E_w w_w,\tag{3a}$$

$$\dot{\eta}_w = C_w \xi,\tag{3b}$$

where $\xi = [\xi_1, \xi_2, \xi_3, \xi_4, \xi_5, \xi_6]^{\mathsf{T}} \in \mathbb{R}^6$, $\eta_w \in \mathbb{R}^3$ is the WF motion vector, $w_w \in \mathbb{R}^3$ is a zero-mean Gaussian white noise vector, $A_w \in \mathbb{R}^{6\times 6}$, $C_w \in \mathbb{R}^{3\times 6}$, and $E_w \in \mathbb{R}^{6\times 3}$ are the system matrix, measurement

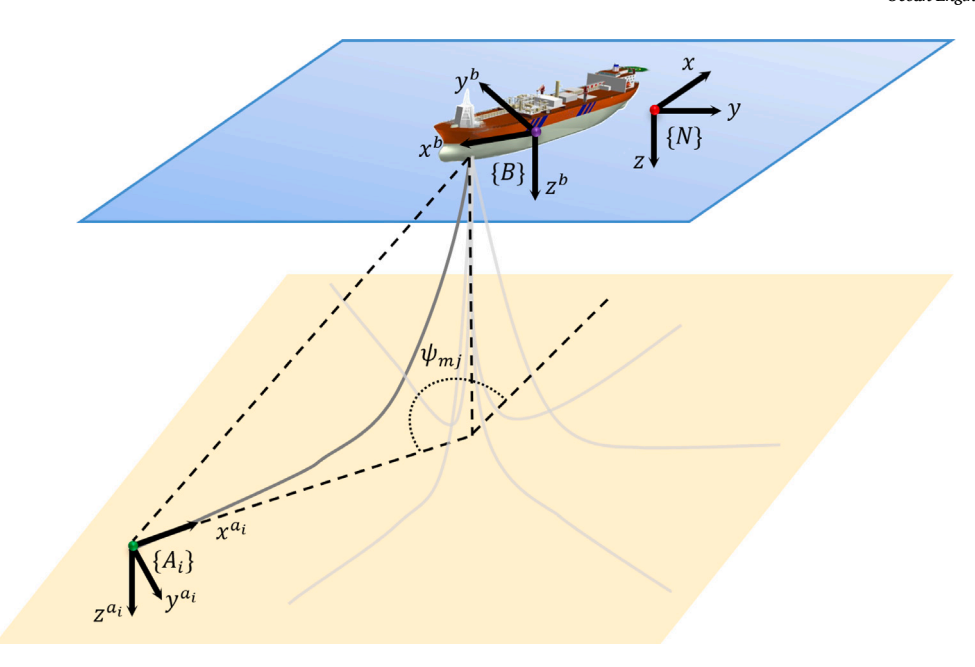


Fig. 1. System configuration and coordinate systems.

matrix, and diagonal scaling matrix of the linear filter, respectively. Specifically, they are

$$A_w = \begin{bmatrix} 0_{3\times3} & I_{3\times3} \\ -\Omega^2 & -2\Delta\Omega \end{bmatrix}, \quad C_w = \begin{bmatrix} 0_{3\times3} & I_{3\times3} \end{bmatrix}, \quad E_w = \begin{bmatrix} 0_{3\times3} \\ K_w \end{bmatrix}, \tag{4}$$

where $\Omega=\mathrm{diag}\{\omega_1,\omega_2,\omega_3\}$, $\Delta=\mathrm{diag}\{\zeta_1,\zeta_2,\zeta_3\}$, $K_w=\mathrm{diag}\{K_{w1},K_{w2},K_{w3}\}$, $\omega_{\{1,2,3\}}$ is the wave frequency, and $\zeta_{\{1,2,3\}}$ is the relative damping chosen between 0.05 and 0.1.

2.3. Mooring line and turret dynamics

The mooring system consists of several mooring lines. The mooring lines provide restoring forces to the turret through fairleads, resulting in horizontal restoring of the moored structure and rotation of the turret. For the LF model, a horizontal-plane spread mooring model is formulated as

$$\tau_m = -R(\psi)^{\mathsf{T}} g_{mo} - d_{mo}(\nu), \tag{5}$$

where g_{mo} denotes the restoring force and moment vector acting at the moored vessel in $\{N\}$, and d_{mo} is the damping effects of the mooring lines, which can be approximated by a linear damping model $d_{mo} = D_{mo}v$. It is a common practice to estimate the linear damping of a mooring line by approximately 10%-20% of the critical damping of the entire system (Nguyen et al., 2011). The linear damping of the mooring system can be augmented into the damping term Dv in Eq. (2c).

The vector of restoring force and moment acting on the moored structure is given by

$$g_{mo} = \begin{bmatrix} g_{mo,1:2}^t \\ D_z^t \hat{\psi}_t \end{bmatrix}, \tag{6}$$

where $g_{mo}^I \in \mathbb{R}^3$ is the restoring force and moment vector acting at the turret, subscript 1: 2 indicates the first and second elements in the vector, D_z^I is the damping between the vessel and the turret, $\tilde{\psi}_t = \psi_t - \psi$ is the relative angle between the turret orientation and vessel heading, and ψ_t is the angle of the turret comparing with the reference x-axis. The dynamic model of $\tilde{\psi}_t$ is given by

$$I_z^t \ddot{\psi}_t = -g_{mo,3}^t - D_z^t \dot{\tilde{\psi}}_t,\tag{7}$$

where I_z^t is the moment of inertia of the turret. The restoring forces and moment vector acting on the turret $g_{mn}^t(\eta) \in \mathbb{R}^3$, which the mooring

lines exert on the turret, is given by

$$g_{mo}^{t} = \sum_{i=1}^{m} \begin{bmatrix} f_{mo,i,1:2} \\ f_{mo,i,1:2} \times (p_{fi} - p_{r}) \end{bmatrix},$$
 (8)

where the superscript and subscript i identify the ith cable, and $f_{mo,i} \in \mathbb{R}^3$ is the generalized force at the end of the cable in $\{N\}$.

The horizontal position of the Anchor i is denoted as p_{ai} . The horizontal position of the fairlead corresponding to Anchor i in $\{N\}$, $p_{fi} = [x_{fi}, y_{fi}]^T \in \mathbb{R}^2$, are given by

$$p_{fi} = p_r + \begin{bmatrix} r_t \cos(\gamma_{fi}) \\ r_t \sin(\gamma_{fi}) \end{bmatrix}, \quad i = 1, \dots, m,$$

$$(9)$$

where $p_r \in \mathbb{R}^2$ is the real-time horizontal position of the COT, which can be replaced by $[x, y]^T$ when the COT overlaps with the center of the vessel; r_t is the radius of the circle where the fairleads locate on COT; and γ_{fi} is the angle of the *i*th fairlead compared to the reference angle.

The mooring lines are simulated by the finite element method (FEM) model (Aamo and Fossen, 2001). Each of the mooring lines is uniformly divided into several segments, and the mass of every segment concentrates at the nodes. The position of the bottom end node is the anchor, and the position of the top end is determined by the fairlead. A node is only influenced by its nearest neighboring nodes and underwater current, including buoyancy, gravity, reaction force, and hydrodynamic drag. The position of each node is initialized by solving the catenary equation.

3. Problem formulation

The objective of this section is to construct a sensor network according to the real-time tension measurement. A tension signal is analogous to a distance measurement.

3.1. Range measurements from tension measurements

Regarding a specific catenary mooring line, the tension exposed to gravity acts as a restoring force on the moored vessel, which is proportional to the displacement of its upper end. An innovative idea is to connect the displacement and tension measurement. It is assumed that a mapping exists between the tension and range in an undisturbed environment. Therefore, we have the following parameter-separation assumption.

Assumption 1. For a catenary mooring line with a fixed anchor at the steady-state, there exists a map $f_i: \mathbb{D}_{X_i} \to \mathbb{R}_+$, such that

$$T_i^0(p_{ai}, p_{fi}, C) = f_i(X_i^0) + \Delta T_{i,c}(C) + \Delta T_{i,c}(p_{fi}) + \Delta T_{i,s}(p_{ai}), i = 1, \dots, m, (10)$$

where T_i^0 is the noiseless axial tension at the top end of the ith mooring line, X_i^0 is the horizontal distance between the ith anchor and the projection of the corresponding fairlead on the seafloor, C is the underwater current profile; and $\Delta T_{i,c}$, $\Delta T_{i,v}$ and $\Delta T_{i,s}$ are the tension deviations due to the current load, wave-induced motion, and seafloor topographical difference from the proposed catenary equation, respectively.

Based on the binary search results of the catenary equations, f_i is a continuously, monotonically and strictly increasing, and local Lipschitz map from the feasible region $\mathbb{D}_{X_i} \subset \mathbb{R}_+$ into the axial tension when heave motion z=0. Hence, f_i is bijective with an inverse function f_i^{-1} . In other words, we can estimate the horizontal projected distance between the anchor and fairlead through a perfect tension measurement, such that $X_i^0 = f_i^{-1}(T_i^0 - \Delta T_{i,c} - \Delta T_{i,s})$. However, this approach is invalid since the tension deviations are not distinguishable in practical situations. Additionally, sensor bias and noise existed in the tension measurement, i.e.,

$$T_i = T_i^0 + b_{ti} + v_{ti}, (11)$$

where $v_{ii} \sim N(0, \sigma_{ii}^2)$ and b_{ti} are the zero-mean Gaussian white noise and sensor bias in the tension measurement of the ith tension cell equipped on the corresponding cable, respectively.

Assumption 2 (*Tension-Range Mapping*). tensionRangeProposition simplified range measurement model from real-time tension measurements with generalized biases and a generalized noise is given by

$$X_i^0 = f_i^{-1}(T_i) + b_{Xi,prop} + b_{Xi,ext} + v_{Xi},$$
(12)

where $v_{Xi} \sim N(0, \sigma_{X_i}^2)$ is the generalized zero-mean Gaussian white noise in the mapping, and $b_{Xi,prop}$ and $b_{Xi,ext}$ are the generalized proprioceptive bias and the exteroceptive bias, respectively.

The model (12) separates uncertainties and environmental influence from f_i . The noise is the superposition of tension-cell sensor noise v_{ti} and dynamic tension $\Delta T_{i,v}$ caused by wave-induced motion. The exteroceptive bias is mainly contributed by the sensor bias b_{ti} in (11). The proprioceptive bias is a generalized effect of the current $\Delta T_{i,c}$ and seafloor $\Delta T_{i,s}$, as well as model uncertainty. When the tension deviation has a linear relation to the horizontal projected distance, the tension noise is also a zero-mean white noise after the mapping.

The feasibility will be discussed as follows.

3.1.1. Noise source 1-wave-frequency motion

To present the influence mechanism of WF motions, the results from the noiseless tension measurement with changing heaves are used as an illustrative example; see Fig. 2. The top end of the mooring line moves 4 meters upward and downward. Suppose that the range is a value at point B, the inverse mapping relies on the red line. When the vessel heaves at z=-4 m, the inverse mapping gives a distance as point A. Similar, the distance appears to stay at point C when z=4 m. The influence is the same for surge and sway motions.

We notice that the influence of v_{Xi} depends on the curve slope and magnitude of the heave motion. The slope of the tension deviation due to heave motion is almost a constant in the neighborhood of a stationary position of the floating vessel. Therefore, the partial derivative of the tension concerning heave motion is almost linear, such that $\frac{\partial T_i^0}{\partial z} \approx \text{constant}$. Since the average heave motion is zero, we assume the dynamic tension from WF motion is an independent zero-mean Gaussian white noise process.

To ensure that the current is independent to this trend, the simulation results from Ren and Skjetne (2016a) with three different current

profiles and motions in $\{A_i\}$ are presented in Fig. 3. From the results, it can be seen that the stiffness is not likely influenced by the current speed significantly. The current profile, to a slight degree, alters the geometrical shape of the mooring line, which then affects the geometric stiffness. The vessel's responses have a more remarkable influence on the tension than the current. We notice that the tension deviation due to vessel motion is independent of neither the current profile form nor the current velocity. The tension deviation is proportional to the surge and heave motions, while the variance caused by the sway motion has an asymmetric property, i.e., the slopes are not straight lines about the sway motion. This result is because the tension deviation compared to the initial value is primary influenced by the elongation of the cable projection on the seafloor, i.e., $\Delta X_i^0 = |p_{fi} - p_{ai}| =$ $\sqrt{(x_{fi}-x_{ai})^2+(y_{fi}-y_{ai})^2-X_{i,init}}$ is nonlinear about y_{fi} , where $X_{i,init}$ is the initial value. As a result, the magnitude of tension deviation caused by sway motion is much smaller than that caused by surge motion. Therefore, the current profile does not influence the aforementioned description, and the floating structure WF motion influences the range measurement as a zero-mean noise with a variance σ_d^2 , which is the same value for all mooring lines. Note that the WF motion-induced tension for various mooring lines is correlated. Since the magnitudes are relatively small, the coupling effects are neglected.

3.1.2. Noise source 2—tension sensor white noise

The tension measurement noise v_{ii} becomes another source of range noise after the inverse map. Based on the low-speed assumption, we consider the generalized stiffness as a constant, i.e.,

$$k_i = \frac{\partial T_i^0}{\partial X_i^0} \Big|_{X_i^0} \simeq \text{constant.}$$
 (13)

Then, the noise contributed by the tension cell sensor is still a zeromean white noise.

Since the sensor noise and WF motion are independent, the noise variance in the range measurement follows the superposition principle. The overall effects can be modeled as Gaussian white noise, and the variance in the projected distance is

$$\sigma_{X_i}^2 = \frac{1}{k^2} (\sigma_{ti}^2 + \sigma_d^2). \tag{14}$$

3.1.3. Bias source 1—seafloor topographical difference and current-induced loads

The seafloor introduces a bias to the tension measurement, i.e., $\Delta T_{i,s}$. To the best of our guess, the seafloor is flat with a known mean depth. However, the seafloor is not perfectly flat due to, for example, reefs or inclines. The mechanics of such an influence are quite similar to the heave motion. When the current profile remains the same in a short-term period, the current load has a constant influence on the mooring line, depending on the difference in orientation between the current direction and the mooring line projection on the seafloor. Therefore, $\Delta T_{i,s}$ can be modeled as a constant bias to the tension measurement.

Additionally, the top tension of a mooring line is influenced by the current-induced load. Hydrodynamic force can be roughly calculated based on a Morison-equation-like form. The tension deviation due to various current velocities and directions is shown in Ren and Skjetne (2016a). From the results, we can find that the influence of a current is approximately quadratically proportional to the magnitude of the current speed.

Note that the current-induced tension deviation $\Delta T_{i,c}$ in a specific current profile is different among mooring lines, even though they all share the same parameters. This is because of the difference in the incoming current direction; see Ren and Skjetne (2016a) for details. Hence, the proportional range bias is given by

$$b_{Xi,prop} = \frac{\Delta T_{i,c} + \Delta T_{i,s}}{k_i}.$$
 (15)

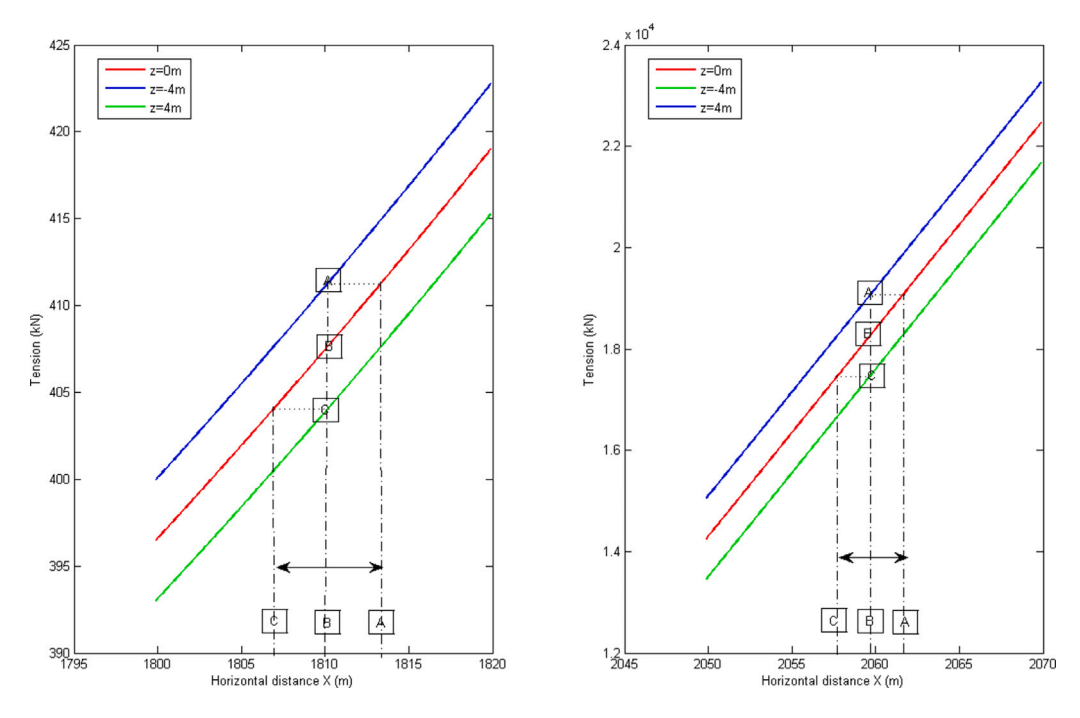


Fig. 2. Influence of the wave-induced heave motion on the generated range signal.

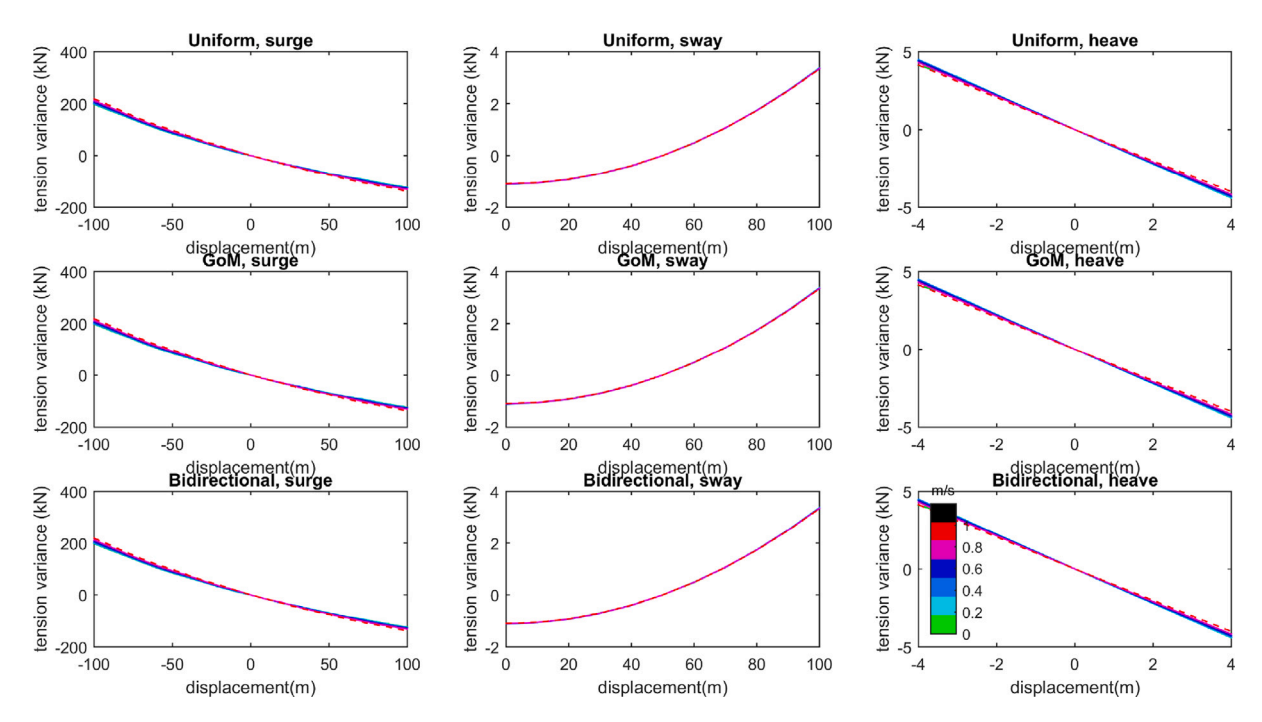


Fig. 3. Axial tension of a mooring line in five specific current profiles.

3.1.4. Bias source 3-tension sensor bias

We assume that the ith exteroceptive sensor bias is fixed to a particular value, which is caused by the initial setup and sensor drift. Hence, the exteroceptive range bias $b_{Xi,ext}$ results from T_{s_i} , such that

$$b_{Xi,ext} = \frac{T_{s_i}}{k_i}. (16)$$

3.2. Line-of-sight assumption

Early studies normally consider a simplified scenario, assuming that all the mooring lines are connected at the COT, e.g., Aamo and Fossen

(1999). Although this is a practical simplification, the influence of the turret and fairleads is not negligible in the proposed application. Assuming that the friction between the turret and the vessel is not negligible, the turret rotates by the sum of the mooring line top torques. Additionally, the magnitude of the turret radius is much smaller than the lengths of the mooring lines. The arrangement is illustrated in Fig. 4. Since the angle $\Delta\psi_{ti}$ is small, we assume the COT is located along with the extension of the line from the anchor to the corresponding fairlead, with a distance r_t from the fairlead, i.e., the distance between the ith anchor and the COT d_i is given by

$$d_i = X_i^0 + r_t + \delta_i, \tag{17}$$

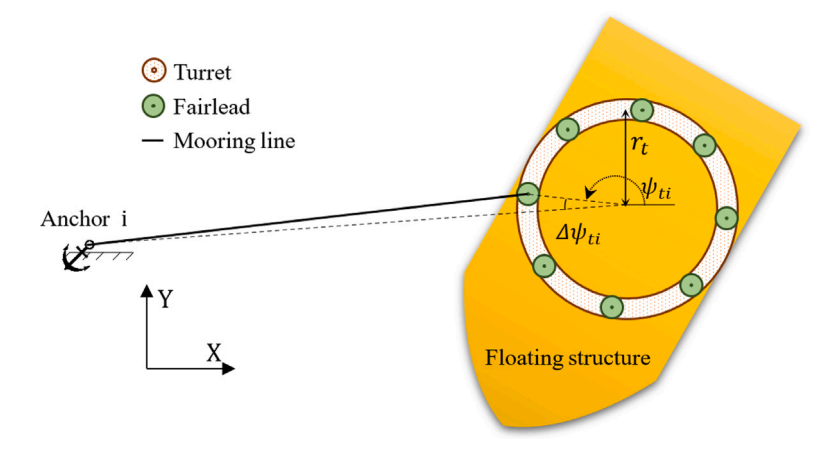


Fig. 4. The fairlead arrangement.

where δ_i is a small error caused by turret rotation.

Remark. The tension deviation is no longer in the form of Gaussian white noise when considering the horizontal motion perpendicular to the cable seafloor projection in y^{a_i} and the natural periods of the WF motions.

The influence due to the current and seafloor is limited when compared to the top tension. For the sake of simplicity, the biases are disregarded in the localization algorithm, i.e., $b_{Xi,prop} = b_{Xi,ext} = \delta_i = 0$. According to the aforementioned discussion, hereafter, the paper is based on the line-of-sight (LOS) assumption.

Assumption 3 (*LOS*). The tension-range mapping is simplified as Assumption 2 and (12). When the length of the suspended mooring line and structural parameter are known, the LOS assumption can be expressed as

$$d_i = f_i^{-1}(T_i) + r_t + v_{X_i}, (18)$$

where f_i is the lookup table generated by setting heave z = 0.

3.3. Sensor network construction

In a specific sea state, a vessel can remain stable around an equilibrium point, where the main environmental loads are balanced by the mooring restoring forces. The equilibrium point is normally determined by the environmental parameters, such as the magnitudes and directions of the second-order wave loads, the current profile, and the mean wind loads. The moving scope for a floating structure is relatively small compared with the mooring line length.

When GNSS signals are available, a floating structure has one beacon (the COT) and m unknown nodes (the anchors). Range-based localization is hence a potential approach as we have a group of m range measurements at any given time instant. However, the application of the algorithm (Ren et al., 2015) is quite limited since it heavily relies on the precise positions of the anchors, but the positions of the anchors are impossible to access with the global navigation satellite system (GNSS) signal due to the signal attenuation in water. In addition, the performance is not satisfied when the anchor positions have full extents of uncertainty. Another practical consideration is that there is no information exchange between the anchors.

A well-known nonlinear passive observer is adopted to filter the measurement noise, eliminate the wave-induced motion, and estimate unmeasured states from position estimate (Fossen and Strand, 1999). The observer is applied to estimate the motion of the moored vessel when the position measurement is available. We collect and store the estimated position and velocity as time series. Here, the observer is well-tuned and the low-frequency motion can be estimated properly.

We assume that the environmental conditions are slow-varying, that is, the equilibrium point for a given short term is constant. The positions from the observers and the tension measurements are collected and stored when the vessel is positioned stably at different equilibrium points. Since the data from the observer is already filtered with respect to noise and WF motion, we can directly read the data at the next time instant in the estimator update process.

Therefore, a sensor network is constructed with n virtual vessels with previously collected and stored time series data, as shown in Fig. 5. In the figure, the virtual vessels are labeled as p_{ij} and $j=1,\ldots,n$. The anchors indexed by from 3 to m-1 are simplified to be a dot-dash line to keep the plot clean. For a practical moored structure, an accepted region is required to protect the mooring system and auxiliary systems (such as risers) from failures. The structure is only allowed to move within the region, resulting in small difference among tension measurements of a same mooring line relevant to different virtual vessels. Consequently, the small difference in the resulting range measurements causes difficulties in a localization problem due to the lack of distinguishability.

3.4. Problem statement

The objective of this paper is then to locate the real-time COT position and unknown anchor positions simultaneously. In the sensor network, n virtual vessels are deemed as known beacons, m fixed anchors with unknown positions, and the real-time vessel COT position is the unknown tracking node. The problem is solvable in the sense of sensor networks.

The mooring line lengths and mean seafloor depth are assumed to be known. Hence, mapping f_i can be calculated according to the catenary equations. If the load of the floating structure changes, the modification should be done to compensate for the influence on f_i . For the sake of simplification, we disregard the water depth and hereafter use a 2D sensor network. The real-time position of the turret and heading vector is $\eta = [p_p^{\ \ \ }, \psi]^{\ \ \ }$ with $p_p = [x_p, y_p]^{\ \ \ }$ is the LF COT position. Note that $p_p \neq p_r$ since the high-frequency wave motion is removed from p_r . The position of the ith anchor and the jth virtual vessel COT are defined as

$$p_{ai} = [x_{ai}, y_{ai}]^{\mathsf{T}}, \quad i = 1, \dots, m,$$
 (19a)

$$p_{tj} = [x_{tj}, y_{tj}]^{\mathsf{T}}, \quad j = 1, \dots, n.$$
 (19b)

Two vectors containing all the anchor positions $p_a \in \mathbb{R}^{2m}$ and turret positions $p_t \in \mathbb{R}^{2n}$ as,

$$p_a = \left[p_{a1}^{\mathsf{T}}, \dots, p_{am}^{\mathsf{T}}\right]^{\mathsf{T}} \text{ and } p_t = \left[p_{t1}^{\mathsf{T}}, \dots, p_{tn}^{\mathsf{T}}\right]^{\mathsf{T}}.$$
 (20)

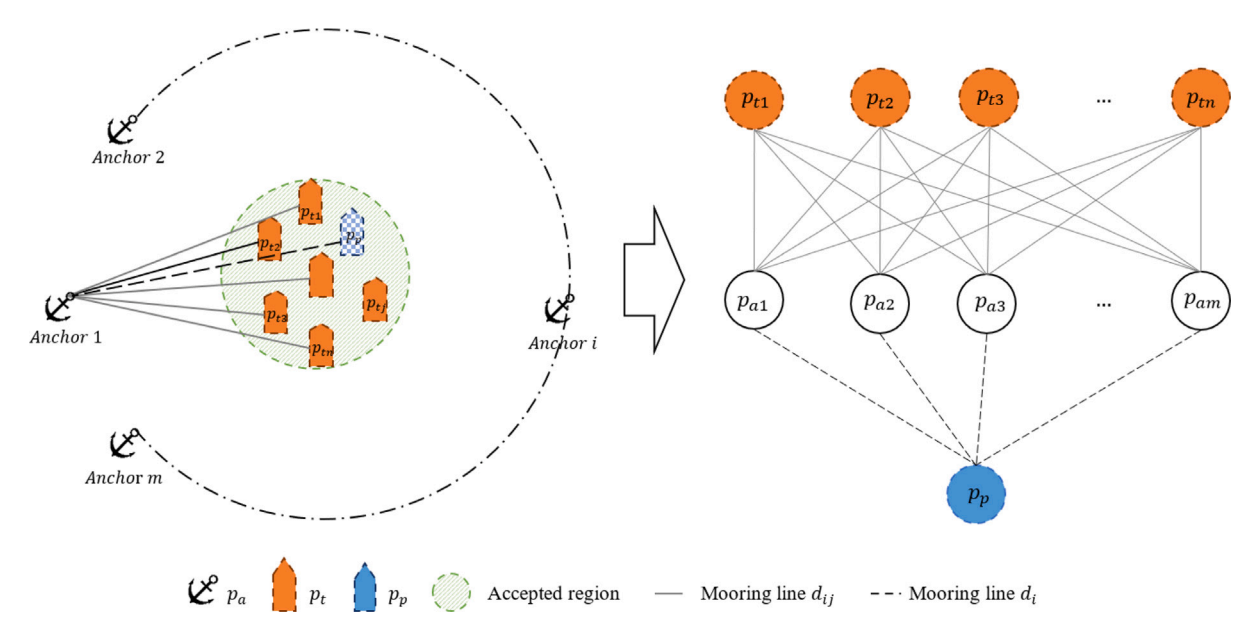


Fig. 5. Analogy sensor network construction (left: system layout in the horizontal plane, right: network topology architecture).

The bias is disregarded by neglecting the current load, sensor bias, and δ_i , i.e., $b_{di}=0$. Similar to Assumption 3, the LOS range between the *i*th anchor and the *j*th virtual vessel COT is given by

$$d_{ij} = f_i^{-1}(T_{ij}) + r_t + v_{Xij}, (21)$$

where
$$v_{Xij} \sim N(0,\sigma_{d_{ij}}^2)$$
, $\sigma_{d_{ij}}^2 = \frac{1}{k_{ij}^2}(\sigma_{ti}^2 + \sigma_{dj}^2)$, and $k_{ij} = \frac{\partial T_{ij}}{\partial X_{ij}^0}\Big|_{X_{ij}^0} \simeq$ constant. Since the moored structure is always running near the equilibrium point, which is determined by the environmental loads, the

 k_i and k_{ij} are in the level of 10⁵ N/m. Then, we define two displacement vectors, $d_I \in \mathbb{R}^m$ and $d_{IJ} \in \mathbb{R}^{mn}$ containing all d_i and d_{ij} , i.e.,

stiffness k_i will not change for a specific virtual vessel. In this case,

$$d_I = [d_1, d_2, \dots, d_m]^{\mathsf{T}},$$
 (22a)

$$d_{IJ} = [d_{11}, d_{12}, \dots, d_{1n}, d_{21}, d_{22}, \dots, d_{2n}, \dots, d_{m1}, d_{m2}, \dots, d_{mn}]^{\mathsf{T}}.$$
 (22b)

The problem is to estimate (p_p,p_a) based on stored (p_t,d_{IJ}) and real-time (d_I,ψ) . There is some available external information in this scenario. First, the lengths of unstretched mooring lines are known by the monitoring system. Moreover, the best initial anchor positions can be received from the installation data and visual observation.

4. Observability analysis

In the network, there are in total m+n+1 nodes, i.e., n beacon nodes with known positions and m+1 nodes with unknown positions. A 2D undirected graph with time-invariant edge is defined as $\mathcal{G}=(\mathcal{V},\mathcal{E})$, where \mathcal{V} are the vortices, $\mathcal{E}=\mathcal{V}\times\mathcal{V}$ are the edges. The total number of edges is mn+m.

If we only consider their transitional motions in the horizontal plane and neglect the rotation and wave-induced motions in the other DOFs, the resulting state equation becomes

$$\begin{bmatrix} \dot{p}_t \\ \dot{p}_a \\ \dot{p}_r \end{bmatrix} = \begin{bmatrix} u_t \\ 0_{2m} \\ u_r \end{bmatrix},$$
 (23)

where the velocity vector is $u_t = [u_{t1}^\top, \dots, u_{tn}^\top]^\top \in \mathbb{R}^{2n}$, and $u_r = [\dot{x}, \dot{y}]^\top \in \mathbb{R}^2$. A new measurement vector is defined as

$$\mathcal{H}(p_t, p_a, p_r) := [p_t^{\mathsf{T}}, \bar{d}_{11}, \bar{d}_{12}, \dots, \bar{d}_{1n}, \dots, \bar{d}_{m1}, \bar{d}_{m2}, \dots, \bar{d}_{mn}, \bar{d}_{1}, \bar{d}_{2}, \dots, \bar{d}_{m}]^{\mathsf{T}},$$

where the squared inter-agent distances are defined as $\bar{d}_i := \frac{1}{2}|p_{ai} - p_r|^2$ and $\bar{d}_{ij} := \frac{1}{2}|p_{ai} - p_{tj}|^2$.

The observability matrix can be calculated by

$$\mathcal{O} = \begin{bmatrix} \nabla \mathcal{L}_{f}^{0}(\mathcal{H}) \\ \nabla \mathcal{L}_{f}^{1}(\mathcal{H}) \\ \vdots \\ \nabla \mathcal{L}_{k}^{k}(\mathcal{H}) \end{bmatrix}$$
(24)

where $\mathcal{L}_f^k(\mathcal{H})$ denotes k-order Lie derivative, i.e., $\mathcal{L}_f^0(\mathcal{H}) = \mathcal{H}$ and $\mathcal{L}_f^k(\mathcal{H}) = (\nabla \mathcal{L}_f^{k-1}(\mathcal{H}))f$ for $k \geq 1$. (See Box I), where $\bar{p}_t = [p_{t1}, p_{t2}, \dots, p_{tn}]^{\mathsf{T}} \in \mathbb{R}^{n \times 2}$, $\bar{p}_a = [p_{a1}, p_{a2}, \dots, p_{an}]^{\mathsf{T}} \in \mathbb{R}^{n \times 2}$, and $\bar{u}_t = [u_{t1}, u_{t2}, \dots, u_{tn}]^{\mathsf{T}} \in \mathbb{R}^{n \times 2}$. After removing the rows of all zeros, the observability matrix becomes a combination of adjust rigidity matrix

$$\mathcal{O} = \begin{bmatrix} A \\ R \\ \mathcal{V} \end{bmatrix} \tag{26}$$

where A, R and U are given in Box II.

The observability in the above-mentioned 2D distance-only localization problem can be proved if the corresponding observability matrix is fully ranked, implying local weak observability.

For a static localization problem ($\bar{u}_t = 0$ and $u_r = 0$ result in $\mathcal{U} = 0$), its solvability can be proved with global rigidity from graph theory, which means distance preserving transformations (Aspnes et al., 2006). Accounting for the movable nodes in the proposed network, the observability matrix is augmented by \mathcal{U} . Hence, it is possible to enhance the rank of the observability matrix with well-selected \bar{u}_t and u_r . We note that the configuration with n=2 also manages to localize the other nodes due to the contributions from \mathcal{U} .

An observability metric from Williams and Sukhatme (2015) is adopted to evaluate the observability, i.e.,

$$\Omega(\mathcal{O}^{\mathsf{T}}\mathcal{O}) = \frac{\lambda_{\min}(\mathcal{O}^{\mathsf{T}}\mathcal{O})}{\lambda_{\max}(\mathcal{O}^{\mathsf{T}}\mathcal{O})}.$$
 (28)

According to the properties of eigenvalues, $\lambda^2(\mathcal{O}) = \lambda(\mathcal{O}^T\mathcal{O}) = \lambda(\mathcal{A}^T\mathcal{A} + \mathcal{R}^T\mathcal{R} + \mathcal{U}^T\mathcal{U})$. Then, Weyl's inequalities are employed to simplify the calculation. Since $(\mathcal{R}^T\mathcal{R})^T = \mathcal{R}^T(\mathcal{R}^T)^T = \mathcal{R}^T\mathcal{R}$, $\mathcal{A}^T\mathcal{A}$, $\mathcal{R}^T\mathcal{R}$, and $\mathcal{U}^T\mathcal{U}$ are Hermitian matrices. In addition, according to the rigidity graph theory, a rigid graph has three eigenvalues to be zeros,

Z. Ren et al. Ocean Engineering 266 (2022) 112706

$$\mathcal{L}_{f}^{0}(\mathcal{H}) = \begin{bmatrix} I_{2n} & 0_{2n\times 2m} & 0_{2n\times 2m} \\ \operatorname{diag}(p_{t1}^{\top} - p_{a1}^{\top}, p_{t2}^{\top} - p_{a1}^{\top}, \dots, p_{tn}^{\top} - p_{a1}^{\top}) \\ \operatorname{diag}(p_{t1}^{\top} - p_{a2}^{\top}, p_{t2}^{\top} - p_{a2}^{\top}, \dots, p_{tn}^{\top} - p_{a2}^{\top}) \\ \vdots \\ \operatorname{diag}(p_{t1}^{\top} - p_{am}^{\top}, p_{t2}^{\top} - p_{ai}^{\top}, \dots, p_{tn}^{\top} - p_{am}^{\top}) \end{bmatrix} & \operatorname{diag}(I_{n} \otimes p_{a1}^{\top} - \bar{p}_{t}, I_{n} \otimes p_{a2}^{\top} - \bar{p}_{t}, \dots, I_{n} \otimes p_{am}^{\top} - \bar{p}_{t}) & 0_{mn\times 2} \\ \vdots \\ \operatorname{diag}(p_{t1}^{\top} - p_{am}^{\top}, p_{t2}^{\top} - p_{ai}^{\top}, \dots, p_{tn}^{\top} - p_{am}^{\top}) \end{bmatrix} & \operatorname{diag}(p_{a1}^{\top} - p_{r}^{\top}, p_{a2}^{\top} - p_{r}^{\top}, \dots, p_{am}^{\top} - p_{r}^{\top}) & 1_{n} \otimes (p_{p})^{\top} - \bar{p}_{a} \end{bmatrix} \\ \nabla \mathcal{L}_{f}^{1}(\mathcal{H}) = \begin{bmatrix} 0_{2n\times 2n} & 0_{2n\times m} & 0_{2n\times m} \\ 0_{m\times 2n} & 0_{2n\times m} & 0_{2n\times 2} \\ 0_{m\times 2n} & -\operatorname{diag}(u_{t1}^{\top}, u_{t2}^{\top}, \dots, u_{tn}^{\top}) & 1_{m} \otimes u_{p}^{\top} \end{bmatrix}$$

$$(25a)$$

$$\nabla \mathcal{L}_{f}^{1}(\mathcal{H}) = \begin{bmatrix} 0_{2n \times 2n} & 0_{2n \times m} & 0_{2n \times 2} \\ 1_{m} \otimes \operatorname{diag}(u_{t_{1}}^{\mathsf{T}}, u_{t_{2}}^{\mathsf{T}}, \dots, u_{t_{n}}^{\mathsf{T}}) & -I_{m} \otimes \bar{u}_{t} & 0_{mn \times 2} \\ 0_{m \times 2n} & -\operatorname{diag}(u_{t_{1}}^{\mathsf{T}}, u_{t_{2}}^{\mathsf{T}}, \dots, u_{t_{n}}^{\mathsf{T}}) & 1_{m} \otimes u_{p}^{\mathsf{T}} \end{bmatrix}$$

$$(25b)$$

$$\nabla \mathcal{L}_f^k(\mathcal{H}) = 0, \ \forall k \ge 2. \tag{25c}$$

Box I.

$$\mathcal{A} = [I_{2n}, 0_{2n \times 2m}, 0_{2n \times 2}], \tag{27a}$$

$$\mathcal{R} = \begin{bmatrix} \operatorname{diag}(p_{t1}^{\top} - p_{a1}^{\top}, p_{t2}^{\top} - p_{a1}^{\top}, \dots, p_{tn}^{\top} - p_{ai}^{\top}) \\ \operatorname{diag}(p_{t1}^{\top} - p_{a2}^{\top}, p_{t2}^{\top} - p_{a2}^{\top}, \dots, p_{tn}^{\top} - p_{a2}^{\top}) \\ \vdots \\ \operatorname{diag}(p_{t1}^{\top} - p_{am}^{\top}, p_{t2}^{\top} - p_{ai}^{\top}, \dots, p_{tn}^{\top} - p_{an}^{\top}) \\ 0_{m \times 2n} \end{bmatrix} diag(I_{n} \otimes p_{a1}^{\top} - \bar{p}_{t}, I_{n} \otimes p_{a2}^{\top} - \bar{p}_{t}, \dots, I_{n} \otimes p_{am}^{\top} - \bar{p}_{t}) \qquad 0_{mn \times 2} \\ \mathcal{U} = \begin{bmatrix} 1_{m} \otimes \operatorname{diag}(u_{t1}^{\top}, u_{t2}^{\top}, \dots, u_{tn}^{\top}) & -I_{m} \otimes \bar{u}_{t} & 0_{mn \times 2} \\ 0_{m \times 2n} & -\operatorname{diag}(u_{t1}^{\top}, u_{t2}^{\top}, \dots, u_{tn}^{\top}) & 1_{m} \otimes u_{p}^{\top} \end{bmatrix}, \tag{276}$$

$$\mathcal{U} = \begin{bmatrix} \mathbf{1}_m \otimes \operatorname{diag}(u_{t1}^\top, u_{t2}^\top, \dots, u_{tn}^\top) & -I_m \otimes \bar{u}_t & \mathbf{0}_{mn \times 2} \\ \mathbf{0}_{m \times 2n} & -\operatorname{diag}(u_{t1}^\top, u_{t2}^\top, \dots, u_{tn}^\top) & \mathbf{1}_m \otimes u_p^\top \end{bmatrix}, \tag{27c}$$

Box II.

i.e., $\lambda_1(\mathcal{R}^{\mathsf{T}}\mathcal{R}) = \lambda_2(\mathcal{R}^{\mathsf{T}}\mathcal{R}) = \lambda_3(\mathcal{R}^{\mathsf{T}}\mathcal{R}) = 0$. By using Lemma 1, we have

$$\lambda_{\min}(\mathcal{O}^{\mathsf{T}}\mathcal{O}) \ge \lambda_{1}(\mathcal{A}^{\mathsf{T}}\mathcal{A}) + \lambda_{4}(\mathcal{R}^{\mathsf{T}}\mathcal{R}) + \lambda_{1}(\mathcal{U}^{\mathsf{T}}\mathcal{U})$$
(29a)

$$\lambda_{\min}(\mathcal{O}^{\mathsf{T}}\mathcal{O}) \le \lambda_{\max}(\mathcal{A}^{\mathsf{T}}\mathcal{A}) + \lambda_{4}(\mathcal{R}^{\mathsf{T}}\mathcal{R}) + \lambda_{\max}(\mathcal{U}^{\mathsf{T}}\mathcal{U})$$
 (29b)

$$\lambda_{\max}(\mathcal{O}^{\mathsf{T}}\mathcal{O}) \ge \lambda_1(\mathcal{A}^{\mathsf{T}}\mathcal{A}) + \lambda_{\max}(\mathcal{R}^{\mathsf{T}}\mathcal{R}) + \lambda_1(\mathcal{U}^{\mathsf{T}}\mathcal{U}) \tag{29c}$$

$$\lambda_{\max}(\mathcal{O}^{\mathsf{T}}\mathcal{O}) \le \lambda_{\max}(\mathcal{A}^{\mathsf{T}}\mathcal{A}) + \lambda_{\max}(\mathcal{R}^{\mathsf{T}}\mathcal{R}) + \lambda_{\max}(\mathcal{U}^{\mathsf{T}}\mathcal{U}) \tag{29d}$$

Since $A^{T}A$ is a diagonal matrix with a 2n number of 1 and a 2(m + n + 1) number of 0 on the main diagonal, the eigenvalues are

$$\lambda_i = \begin{cases} 0, & \text{if } i = 1, \dots, 2m + 2\\ 1, & \text{if } i = 2m + 3, \dots, 2(m + n + 1). \end{cases}$$

Substituting into (29) yields

$$\lambda_4(\mathcal{R}^{\top}\mathcal{R}) + \lambda_{\min}(\mathcal{U}^{\top}\mathcal{U}) \le \lambda_{\min}(\mathcal{O}^{\top}\mathcal{O}) \le 1 + \lambda_4(\mathcal{R}^{\top}\mathcal{R}) + \lambda_{\max}(\mathcal{U}^{\top}\mathcal{U}), \tag{30a}$$

$$\lambda_{\max}(\mathcal{R}^{\top}\mathcal{R}) + \lambda_{\min}(\mathcal{U}^{\top}\mathcal{U}) \le \lambda_{\max}(\mathcal{O}^{\top}\mathcal{O}) \le 1 + \lambda_{\max}(\mathcal{R}^{\top}\mathcal{R}) + \lambda_{\max}(\mathcal{U}^{\top}\mathcal{U}).$$
(30b)

Substituting (30) into (28), we have

$$\frac{\lambda_{4}(R^{\top}R) + \lambda_{\min}(\mathcal{U}^{\top}\mathcal{U})}{1 + \lambda_{\max}(R^{\top}R) + \lambda_{\max}(\mathcal{U}^{\top}\mathcal{U})} \leq \Omega(\mathcal{O}) \leq \frac{1 + \lambda_{4}(R^{\top}R) + \lambda_{\max}(\mathcal{U}^{\top}\mathcal{U})}{\lambda_{\max}(R^{\top}R) + \lambda_{\min}(\mathcal{U}^{\top}\mathcal{U})}.$$
(31)

A practical concern is that the mooring projection lengths ($\bar{p}_a - \bar{p}_t$ and $\bar{p}_a - \bar{p}_p$) normally are much larger than the values of velocities $(\bar{u}_t \text{ and } u_r)$. Compared to the graph topology \mathcal{A} and actuation \mathcal{U} , the network configuration contributes most to the observability. Therefore, we hereafter focus on the rigidity matrix.

Note that the metric does not indicate which network configuration is better, but only a way to present the metric. It is possible to improve the observability by changing the mooring line configuration, e.g., reduce $\lambda_{\max}(\mathcal{R}^{\top}\mathcal{R})$.

The influence of the network configuration is illustrated in Figs. 6–7. In the illustrative scenario, the anchors and virtual vessels are assumed to be evenly distributed in a circle with the same angular interval, respectively. The left column only shows the illustrative layout with m = 5 and n = 3. Furthermore, normalized distribution radii are used, where $p_a = \frac{r_a}{r_t} [\cos \frac{2\pi(i-1)}{m}, \sin \frac{2\pi(i-1)}{m}]^{\mathsf{T}}$ for $i=1,\ldots,m$ and $p_t = [\cos \frac{2\pi(j-0.5)}{n}, \sin \frac{2\pi(j-0.5)}{n}]^{\mathsf{T}}$ for $j=1,\ldots,n$, where r_a and r_t are the radii of distribution circles for the anchors and virtual vessels, respectively. From Eqs. (28) and (27b), it is easy to note that the proportion between the two radii, instead of their absolute values, influences the results of $\lambda(\mathcal{R}^{\mathsf{T}}\mathcal{R})$. There is a half interval lag for the virtual vessel distribution. The real-time vessel stays at the origin $p_r = [0, 0]^T$. From Fig. 6, another way to enhance the observability is to increase the value of $\frac{r_a}{r_a}$.

It is concluded that the network should have a number of at least 3 anchors and 3 virtual vessels to maintain the rigidity (observability). In addition, the observability is improved with an increasing number of virtual vessels. Different configuration has different trend.

5. Simultaneous localization of anchors and moored vessel

Regarding the sensor network built in Section 3.3, the stored vessel position data p_t , stored tension data, real-time heading, and online tension measurements are available. To simplify the representation, we employ the range measurements directly after the tension mapping, i.e., d_I and d_{IJ} . The anchors have fixed positions, but noise is needed to balance the distance between the estimated and real positions, which is similar to (2b), applied to simulate the slow-varying loads. The discrete form is given by

$$p_{ai}(k+1) = p_{ai}(k) + w_{ai}, (32)$$

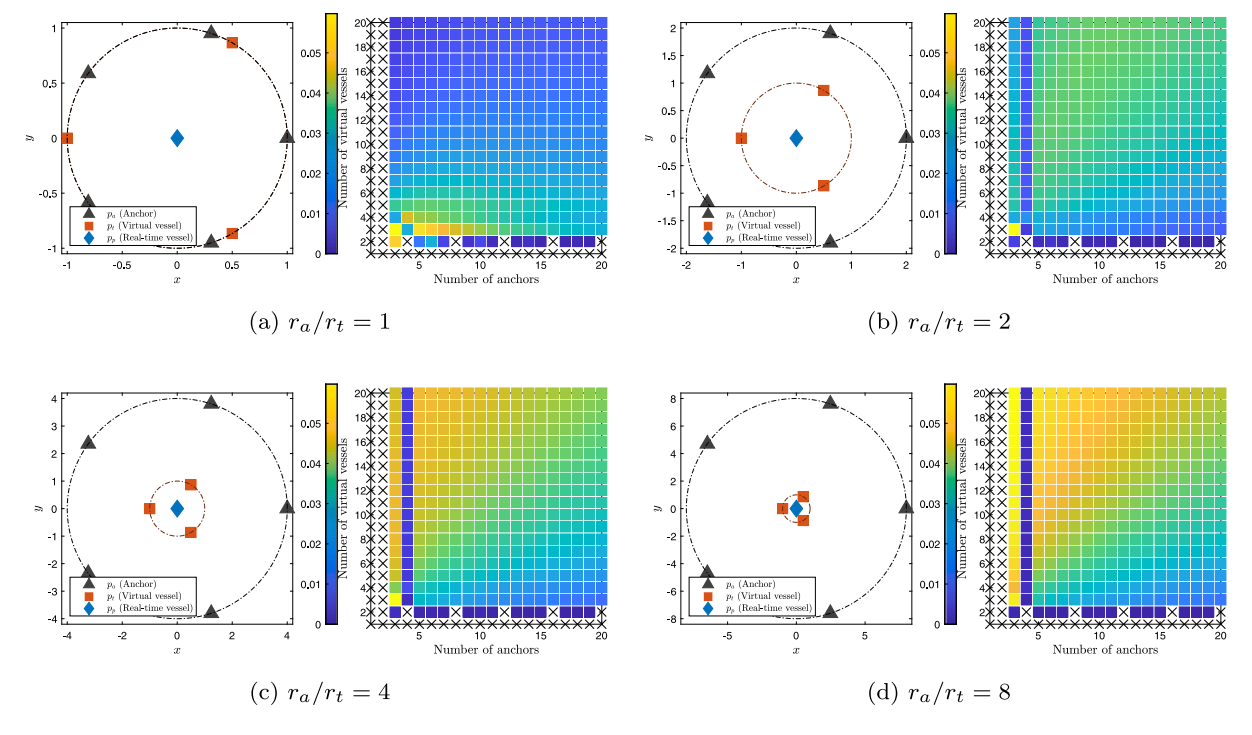


Fig. 6. $\Omega(R^TR)$ with different numbers of anchors and virtual vessels (distributed along circles).

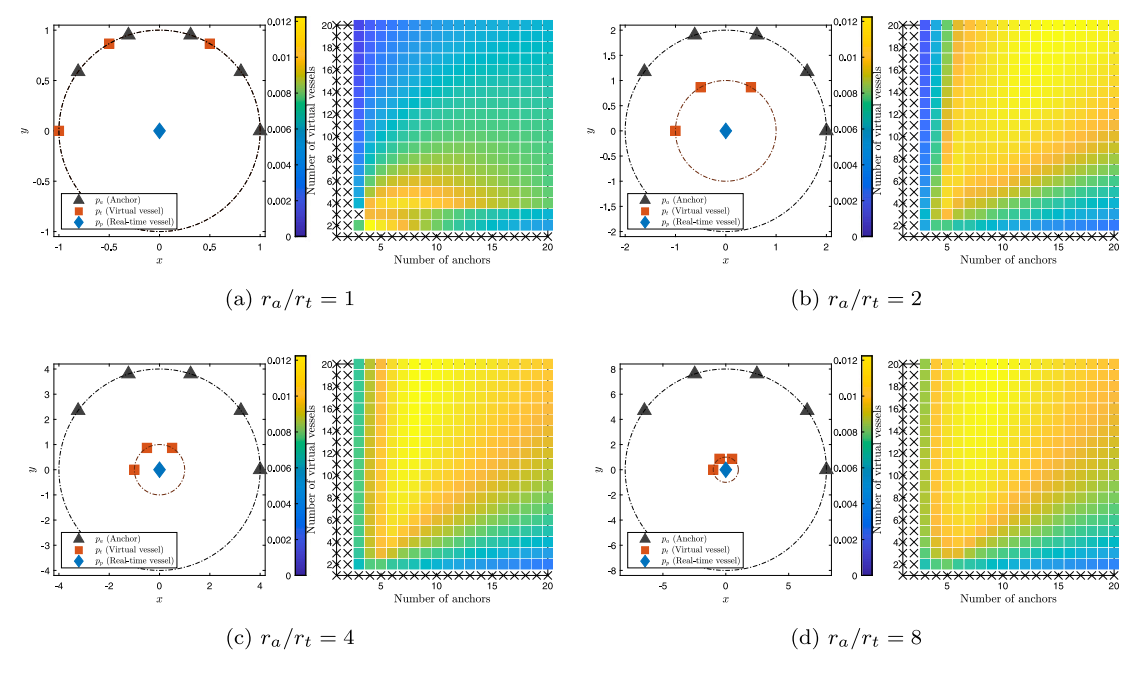


Fig. 7. $\Omega(R^TR)$ with different numbers of anchors and virtual vessels (distributed along half circles).

where w_{ai} is a zero-mean noise. The continuous form is given by

$$\dot{p}_a = E_a \omega_a. \tag{33}$$

where $E_a \in \mathbb{R}^{2m \times 2m}$ is an identity matrix and $\omega_a = [w_{a1}, \dots, w_{am}]^{\mathsf{T}}$.

Theorem 2 (State Space Equation for a Moored Structure with Only Tension Measurements and Magnetometer.). The overall EKF is based on

the nonlinear complete model

$$f(\mathbf{x}) = \begin{bmatrix} A_w \xi \\ R(\psi)v \\ -T_b^{-1}b \\ -M^{-1}Dv + M^{-1}R^{\mathsf{T}}(\psi)b - M^{-1}R^{\mathsf{T}}(\psi)g_{mo} \\ 0_{2m} \\ 0_{2n} \end{bmatrix},$$
(34)

$$B = \begin{bmatrix} 0_{6\times3} \\ 0_{3\times3} \\ 0_{3\times3} \\ M^{-1} \\ 0_{2m\times3} \\ 0_{2n\times3} \end{bmatrix}, \qquad E = \begin{bmatrix} E_{w} & 0_{3\times3} & 0_{6\times2m} \\ 0_{3\times3} & 0_{3\times3} & 0_{3\times2m} \\ 0_{3\times3} & E_{b} & 0_{3\times2m} \\ 0_{2m\times3} & 0_{2m\times3} & 0_{2m\times3} & E_{a} \\ 0_{2n\times3} & 0_{2n\times3} & 0_{2n\times2m} \end{bmatrix},$$

$$h(\mathbf{x}) = \begin{bmatrix} \psi + \xi_6 \\ p_t \\ G_I(p_a, \eta) \\ G_{IJ}(p_a, p_t) \end{bmatrix}, \tag{35}$$

where the state vector is $\mathbf{x} = [\boldsymbol{\xi}^{\mathsf{T}}, \boldsymbol{\eta}^{\mathsf{T}}, b^{\mathsf{T}}, v^{\mathsf{T}}, x_a^{\mathsf{T}}, x_t^{\mathsf{T}}]^{\mathsf{T}}, \ \boldsymbol{\eta} = [p_p^{\;\mathsf{T}}, \psi]^{\mathsf{T}}, \ \text{the}$ measurement vector is $\mathbf{y} = [\psi + \boldsymbol{\xi}_6, p_t^{\;\mathsf{T}}, d_I^{\;\mathsf{T}}, d_{IJ}^{\;\mathsf{T}}]^{\mathsf{T}}, \ w = [w_w^{\mathsf{T}}, w_b^{\mathsf{T}}, w_a^{\mathsf{T}}]^{\mathsf{T}},$ and $\mathbf{u} = \tau_c$.

The tuning matrices are $Q \in \mathbb{R}^{(6+2m)\times(6+2m)}$ and $R \in \mathbb{R}^{(1+2n+m+mn)\times(1+2n+m+mn)}$. The distance mapping functions are given by

$$d_I = G_I(p_a, p_p + [\xi_4, \xi_5]^{\mathsf{T}}), \quad \text{and} \quad d_{IJ} = G_{IJ}(p_a, p_t),$$
 (36)

where the estimated distances are given by

$$d_i = g_i(p_{ai}, p_p + [\xi_4, \xi_5]^{\mathsf{T}}) = \sqrt{(x_{ai} - x_p - \xi_4)^2 + (y_{ai} - y_p - \xi_5)^2},$$
 (37a)

$$d_{ij} = g_{ij}(p_{ai}, p_{tj}) = \sqrt{(x_{ai} - x_{jt})^2 + (y_{ai} - y_{tj})^2}.$$
 (37b)

The Jacobian matrix is given by

$$H = \frac{\partial h}{\partial x} = \begin{bmatrix} \frac{\partial \psi_w}{\partial \xi} & \frac{\partial \psi_w}{\partial \eta} & 0_{1\times 3} & 0_{1\times 3} & 0_{1\times 2m} & 0_{2n\times 2n} \\ 0_{2n\times 6} & 0_{2n\times 3} & 0_{2n\times 3} & 0_{2n\times 3} & 0_{2n\times 2m} & I_{2n\times 2n} \\ \frac{\partial d_I}{\partial \xi} & \frac{\partial d_I}{\partial \eta} & 0_{m\times 3} & 0_{m\times 3} & \frac{\partial d_I}{\partial p_a} & 0_{m\times 2n} \\ 0_{mn\times 6} & 0_{mn\times 3} & 0_{mn\times 3} & 0_{mn\times 3} & \frac{\partial d_{IJ}}{\partial p_a} & \frac{\partial d_{IJ}}{\partial p_t} \end{bmatrix}.$$
(38)

where

$$\frac{\partial \psi}{\partial \xi} = \begin{bmatrix} 0 & 0 & 0 & 0 & 0 & 1 \end{bmatrix}, \quad \frac{\partial \psi}{\partial n} = \begin{bmatrix} 0 & 0 & 1 \end{bmatrix}, \tag{39a}$$

$$\frac{\partial d_I}{\partial \xi} = \begin{bmatrix} 0_{m \times 3}, & A_1 A_2 A_3, & 0_m \end{bmatrix}, \quad \frac{\partial d_I}{\partial n} = \begin{bmatrix} A_1 A_2 A_3, & 0_m \end{bmatrix}, \tag{39b}$$

where $A_1 = \operatorname{diag}\{\frac{1}{d_1}, \frac{1}{d_2}, \dots, \frac{1}{d_m}\}, A_2 = [1_{m \times 2}, -I_{m \times m}], A_3 = [p_p, [\xi_4, \xi_5]^\top, p_{1a}, p_{2a}, \dots, p_{am}]^\top,$

$$\frac{\partial d_I}{\partial p_a} = \begin{bmatrix} \chi_1 & 0_2 & \cdots & 0_2 \\ 0_2 & \chi_2 & \cdots & 0_2 \\ \vdots & \vdots & \ddots & \vdots \\ 0_2 & 0_2 & \cdots & \chi_m \end{bmatrix}, \ \chi_i = \begin{bmatrix} \frac{x_p + \xi_4 - x_{ai}}{d_i} & \frac{y_p + \xi_5 - y_{ai}}{d_i} \end{bmatrix}, \tag{39c}$$

$$\frac{\partial d_{IJ}}{\partial p_{a}} = \begin{bmatrix}
\varsigma_{1} & 0_{n \times 2} & \cdots & 0_{n \times 2} \\
0_{n \times 2} & \varsigma_{2} & \cdots & 0_{n \times 2} \\
\vdots & \vdots & \ddots & \vdots \\
0_{n \times 2} & 0_{n \times 2} & \cdots & \varsigma_{m}
\end{bmatrix}, \zeta_{i} = \begin{bmatrix}
\frac{x_{ai} - x_{I1}}{d_{i1}} & \frac{y_{ai} - y_{I1}}{d_{i1}} \\
\frac{x_{ai} - x_{I2}}{d_{i2}} & \frac{y_{ai} - y_{I2}}{d_{i2}} \\
\vdots & \vdots \\
\frac{x_{ai} - x_{I1}}{d_{i1}} & \frac{y_{ai} - y_{I1}}{d_{i1}}
\end{bmatrix} \tag{39d}$$

$$\frac{\partial d_{IJ}}{\partial p_t} = \begin{bmatrix} \theta_1 \\ \theta_2 \\ \vdots \\ \theta_m \end{bmatrix}, \\
\theta_i = \begin{bmatrix} \frac{x_{t1} - x_{ai}}{d_{i1}} & \frac{y_{t1} - y_{ai}}{d_{i1}} & \frac{x_{t2} - x_{ai}}{d_{i2}} & \frac{y_{t2} - y_{ai}}{d_{i2}} & \\ & & & \ddots & \\ & & & & \frac{x_{m} - x_{ai}}{d_{in}} & \frac{y_{tn} - y_{ai}}{d_{in}} \end{bmatrix}$$
(39e)

Remark. We notice that the matrices $\frac{\partial d_{IJ}}{\partial p_a}$ and $\frac{\partial d_{IJ}}{\partial p_t}$ are made up of n blocks. To write it in this form has the advantage that every block is related to one anchor. In other words, we can choose the relevant anchors to construct the matrices.

In practice, we may have more available information than the model we introduced. For instance, when the anchor positions are all well-known, we may only estimate the position of the vessel based on the tension measurements. This model will be presented in Lemma 3. Furthermore, the only interesting information may be the location of the anchor when the vessel has lost the anchor. This simplified model will be depicted in Lemma 4. In these models, the structures of the sensor network also vary.

Lemma 3 (Simplified Model 1. Vessel Localization with Known Anchor Positions and Real-Time Tension Measurement). When the anchor positions are known, the goal is to estimate the LF motion of the moored vessel p_p with tension measurements. The state vector hence is $\mathbf{x} = [\boldsymbol{\xi}^\mathsf{T}, \boldsymbol{\eta}^\mathsf{T}, b^\mathsf{T}, \boldsymbol{v}^\mathsf{T}]^\mathsf{T}$, the observation vector is $\mathbf{y} = [\boldsymbol{\psi}, \boldsymbol{d}_I^\mathsf{T}]^\mathsf{T}$, the disturbance vector is $\mathbf{w} = [\boldsymbol{w}_w^\mathsf{T}, \boldsymbol{w}_b^\mathsf{T}]^\mathsf{T}$, $\mathbf{u} = \tau_c$, and the estimated distance is given by $\hat{d}_i = g_{ij}(p_{ai}, \hat{p}_p)$. Then the key matrices in the algorithm are simplified as

$$f(\mathbf{x}) = \begin{bmatrix} A_w \xi \\ R(\psi)v \\ -T_b^{-1}b \\ -m^{-1}Dv + m^{-1}R(\psi)^{\mathsf{T}}b - m^{-1}R^{\mathsf{T}}(\psi)g_{mo} \end{bmatrix}, \tag{40}$$

$$B = \begin{bmatrix} 0_{6\times3} \\ 0_{3\times3} \\ 0_{3\times3} \\ m^{-1} \end{bmatrix}, \qquad E = \begin{bmatrix} E_w & 0_{3\times3} \\ 0_{3\times3} & 0_{3\times3} \\ 0_{3\times3} & E_b \\ 0_{3\times3} & 0_{3\times3} \end{bmatrix}, \qquad h(\mathbf{x}) = \begin{bmatrix} \psi + \xi_6 \\ G_I(p_a, \eta) \end{bmatrix}, \tag{41}$$

The Jacobian matrix is given by

$$H = \frac{\partial h}{\partial x} = \begin{bmatrix} \frac{\partial \psi}{\partial \xi} & \frac{\partial \psi}{\partial \eta} & 0_{1\times 3} & 0_{1\times 3} \\ \frac{\partial d_I}{\partial \xi} & \frac{\partial d_I}{\partial \eta} & 0_{m\times 3} & 0_{m\times 3} \end{bmatrix}.$$
(42)

Lemma 4 (Simplified Model 2. Unknown Anchors Localization with GNSS-Assist). Another simplified form is to only estimated the anchors. The state vector is $\mathbf{x} = [x_a^{\mathsf{T}}, p_t^{\mathsf{T}}]^{\mathsf{T}}$, the observation vector is $\mathbf{y} = [p_t^{\mathsf{T}}, d_{IJ}^{\mathsf{T}}]^{\mathsf{T}}$, and the estimated distance is given by $\hat{d}_{ij} = g_{ij}(\hat{p}_{ai}, p_{tj})$. The state-space form is formulated as

$$\dot{\mathbf{x}} = Ew_a,
\mathbf{y} = h(\mathbf{x}) + v,$$
(43)

where

$$E = \begin{bmatrix} E_a \\ 0_{2n \times 2m} \end{bmatrix}, \qquad h(x) = \begin{bmatrix} x_t \\ G_{IJ}(p_a, p_t) \end{bmatrix}, \tag{44}$$

The Jacobian matrix is given by

$$H = \frac{\partial h}{\partial x} = \begin{bmatrix} 0_{2n \times 2m} & I_{2n \times 2n} \\ \frac{\partial d_{IJ}}{\partial p_n} & \frac{\partial d_{IJ}}{\partial p_t} \end{bmatrix}. \tag{45}$$

In the sensor network, the anchors are independent. In other words, we can detect arbitrary anchors. Therefore, this network applies to all vessels equipped with tension cells. For the sake of simplification, the typical EKF is not repeated here.

Range measurements d_{IJ} depend on the positions of the virtual vessel and anchors, and the range measurement d_I is dependent on the anchor position and real-time estimated vessel position.

Table 1
Vessel main particulars

vesser main particulars.		
Principle dimension	Unit	Values
Vessel Type		FPSO
Length between perp.	m	200
Molded breadth	m	44
Draught	m	12
Mass	ton	1.004e5
Position of COG	m	[0,0,11]
Radius of turret r_t	m	20

Table 2 Mooring line dimensions.

Principle dimension	Unit	Values	
Density of ambient water	kg/m³	1025	
Density of cable	kg/m	275	
Length of the cable	m	2350	
Elastic modulus E	Pa	2×10^{10}	
Cable cross section area	m^2	0.04	
Cable diameter	m	0.08	
Max strain ϵ	-	0.005	
Normal drag coefficient	-	0.3	
Tangential drag coefficient	-	1.0	

6. Numerical simulation

6.1. Overview

The simulations are conducted in MATLAB/Simulink® with the MSS toolbox (MSS. Marine Systems Simulator, 2010) and MarIn toolbox (Ren et al., 2018). The parameters of the mooring lines and a moored FPSO are tabulated in Tables 1 and 2. The sampling interval is 0.02 s. Nonlinear dynamics are considered in the simulations.

To collect time-series data for the virtual vessels, a group of simulations in various environments are conducted, as listed in Table 4.

All the environmental parameters are generated randomly, including the wind speed and direction, the significant wave height and its main direction, the current speed and direction, and the estimated initial anchor positions. The peak wave period is set to be 7 s, and an irregular wave condition is simulated using an ITTC spectrum. The current profile is a linear interpolation of preset current speeds at water depths 0, 250 m, 500 m, 750 m, and 1000 m, respectively. In the scenario with only surface current, the current speeds (v_{cur}) at water depths 250 m, 500 m, 750 m, and 1000 m are set to be zeros. The current direction remains the same along water depth and the value is randomly set in a $\pm 35deg$ region from the main wave direction.

Data are only collected after the vessel has been stabilized at a new equilibrium point given by the different environmental parameters, even though the vessels can never become fixed due to the time-varying loads. Then, we have a set of virtual vessels running in different environments at a group of equilibrium points, where the equilibrium positions in Table 4 are the mean values over the period. By comparing the second and third columns in Table 4, the current profiles only slightly influence the positions of the equilibrium points.

Monte Carlo simulations are conducted using the generated data, which contain n virtual and 1 real-time measurement, and selecting n sets of data from 20 sets of simulation results. To test the influence of the number n, we select 10 groups of data; see Table 3. For each group, there are four virtual vessels randomly selected if n=4. When n=7, three additional virtual vessels are added. Another three virtual vessels are introduced when N=10. For each simulation, a set of data is selected from the rest of the sets as the real-time measurement. There are five simulations for each group of n, i.e., the numbers under (I)–(V) in Table 3 are the indices of simulations used as the real-time measurement. The simulations last for 1000 s.

Sensitivity studies are conducted to verify the estimation performance. To verify the robustness of this algorithm, we assume noise with

high variance in the tension cells, e.g., $\sigma_{ti}^2 = 10^8$, which is much larger than in a practical situation. The tension measurement is quite noisy here. Hence, the distance from the mapping suffers greatly from noise.

6.2. Simulation results

The time-domain simulation results are, for example, shown in Figs. 8–9. We determine that the anchor positions and the real-time COT motion are well estimated. The performance mainly depends on the parametric tuning and variances of the noise in the tension measurements. Furthermore, the computational time depends on the number of virtual vessels.

In the initial 5 seconds, the COT position estimates \hat{p}_p quickly converge to the real value p_p . The convergence rate enhances with n. Then, the COT position estimates are closed to the real value. With only surface current, the COT position estimate oscillates around the real value with an error of less than 1 m. The estimation performances for n=7 and n=10 are similar. The current profile introduces a constant bias in both directions. An oscillation is noticed in the estimates with the main wave frequency. The reason for the oscillation is primarily due to the mooring line motions resulting from the vessel's wave-induced motions. The virtual vessel is influenced by the WF motion, which is removed from p_t . Another minor source is the turret rotational dynamics.

The anchor position p_t quickly converges and remains bounded around the real positions. The convergence speed largely depends on the choice of the matrices, such as E_a , Q and R. With the same E_a , the convergence speed is faster with an increasing number of virtual vessels. The computational speed is enhanced quadratically.

The simulation results agree with the expectation, showing that the estimation of the anchor positions is slower than the real-time localization of the moored vessel. With only surface current, the anchor position estimate has a bias of fewer than 10 m. The difference among different ns is limited. When the current profile is involved, a bias is introduced in the estimate. For specific anchors, e.g., Anchors 3 and 7, the estimated biases for various values of n are similar. However, the bias differences are large for other anchor position estimates. The bias decreases with increasing n from n = 4 to n = 7.

6.3. Comparison study

The biases and mean square errors(MSEs) of the position estimates at the COT and *i*th anchor are respectively defined as

$$b_t = \frac{1}{n_t} \sum_{k=1}^{n_t} |p_p - \hat{p}_p|, \tag{46a}$$

$$MSE_{t} = \frac{1}{n_{t}} \sum_{k=1}^{n_{t}} (|p_{p} - \hat{p}_{p}| - b_{t})^{2},$$
(46b)

$$b_{ai} = \frac{1}{n_t} \sum_{k=1}^{n_t} |p_{ai} - \hat{p}_{ai}|, \ i = 1, \dots, m,$$
 (46c)

$$MSE_{ai} = \frac{1}{n_t} \sum_{k=1}^{n_t} (|p_{ai} - \hat{p}_{ai}| - b_{ai})^2,$$
 (46d)

where n_t is the number of total sampling intervals.

The simulation results are presented in Figs. 10–11. The bar graphs for the anchors illustrate the mean value of the estimates. The values for specific anchors are presented with markers. Current profiles influence the estimation performance remarkably. The estimated bias is less than 2.5 meters with the current profile. The improvement of increasing n to the COT position estimates is not significant. However, biases for the anchor position estimates are reduced with increasing n. The MSE for the anchor position estimate is larger than that of the COT, possibly because the current-induced loads acting on different mooring lines compensate for other effects in the estimator. When n = 4, the estimation performance is not perfectly stable. For some anchors, the

 Table 3

 Run time with a different number of virtual vessels.

Simulation	Virtual vessel indices			Real-time vessel index				
group no.	n=4	n = 7	n = 10	(I)	(II)	(III)	(IV)	(V)
(a)	3 5 6 9	11 13 19	4 8 16	15	7	12	14	18
(b)	2 4 5 16	1 3 18	7 17 19	8	13	20	9	10
(c)	5 3 20 6	1 16 18	7 14 15	19	2	12	17	13
(d)	3 9 13 20	1 7 11	14 15 16	12	8	5	2	18
(e)	2 4 8 10	157	6 15 17	9	18	12	20	11
(f)	4 9 18 13	1 5 10	6 7 19	17	14	15	11	16
(g)	1 4 7 19	3 8 10	9 11 17	20	18	12	13	2
(h)	10 15 18 19	3 5 20	2 12 14	9	6	7	16	13
(i)	2 8 16 17	11 18 19	5 9 13	7	3	20	6	14
(j)	1 3 4 7	5 10 15	9 16 17	13	8	19	20	14

Table 4
Vessel equilibrium points

Index	Equilibrium position		Wind	Waves	Current profile depth [0,250,500,750,1000] (m)		
[<i>j</i>]	with only surface current $[x_{ij}, y_{ij}]^{T}$ (m)	with current profile $[x_{ij}, y_{ij}]^T$ (m)	$ \frac{[\nu_{wind}, \beta_{wind}]}{(\text{m/s,deg})} $	$ \frac{[H_s, \beta_{wave}]}{(m, deg)} $	v _{cur} (m/s)	β_{cur} (deg)	
1	[3.9, -122.0]	[6.4, -122.0]	[2.5, 98.0]	[2.1, 87.0]	[0.8, 0.048, 0.34, 0.2, 0.77]	43.0	
2	[39.0, -57.0]	[40.0, -51.0]	[5.8, 122.0]	[1.6, 111.0]	[0.44, 0.38, 0.97, 0.59, 0.3]	100.0	
3	[6.9, -144.0]	[1.6, -144.0]	[5.2, 43.0]	[0.76, 79.0]	[0.98, 0.41, 0.48, 0.95, 0.18]	144.0	
4	[0.94, -15.0]	[2.9, -11.0]	[1.6, 40.0]	[2.3, 89.0]	[0.096, 0.4, 0.37, 0.26, 0.69]	32.0	
5	[-58.0, -59.0]	[-53.0, -54.0]	[4.9, 93.0]	[0.3, 41.0]	[0.53, 0.42, 0.76, 0.51, 0.26]	43.0	
6	[38.0, -76.0]	[39.0, -74.0]	[5.0, 77.0]	[3.0, 111.0]	[0.55, 0.38, 0.38, 0.64, 0.46]	97.0	
7	[-32.0, -30.0]	[-26.0, -19.0]	[8.4, 6.2]	[0.72, 42.0]	[0.28, 0.91, 0.9, 0.4, 0.84]	10.0	
8	[-58.0, -5.8]	[-53.0, 1.1]	[8.1, -47.0]	[0.58, 7.1]	[0.37, 0.67, 0.18, 0.49, 0.88]	-14.0	
9	[2.6, -9.6]	[-0.37, -17.0]	[8.6, 99.0]	[2.0, 86.0]	[0.065, 0.96, 0.37, 0.75, 0.7]	177.0	
10	[57.0, -66.0]	[56.0, -70.0]	[6.1, 122.0]	[0.1, 111.0]	[0.54, 0.16, 0.92, 0.13, 0.76]	177.0	
11	[-111.0, -58.0]	[-100.0, -55.0]	[5.7, -30.0]	[1.1, 19.0]	[0.84, 0.75, 0.52, 0.043, 0.97]	88.0	
12	[-13.0, -18.0]	[-11.0, -17.0]	[6.1, 66.0]	[0.93, 50.0]	[0.15, 0.37, 0.09, 0.37, 0.4]	42.0	
13	[-26.0, -8.3]	[-22.0, -5.1]	[1.0, 4.4]	[0.23, 11.0]	[0.17, 0.45, 0.74, 0.69, 0.13]	65.0	
14	[-6.9, -9.1]	[0.98, -1.6]	[1.6, 2.0]	[0.38, 54.0]	[0.068. 0.039, 4.7e-3, 0.94, 0.72]	-12.0	
15	[36.0, -122.0]	[41.0, -111.0]	[4.1, 89.0]	[1.3, 100.0]	[0.82, 0.56, 0.6, 0.48, 0.9]	26.0	
16	[-13.0, -16.0]	[-12.0, -14.0]	[5.6, 17.0]	[2.6, 47.0]	[0.13, 0.37, 0.96, 0.13, 0.17]	25.0	
17	[-111.0, -68.0]	[-111.0, -65.0]	[2.7, 81.0]	[2.7, 30.0]	[0.88, 0.79, 0.4, 0.48, 0.043]	7.6	
18	[-55.0, -58.0]	[-44.0, -49.0]	[7.8, 58.0]	[0.17, 43.0]	[0.51, 0.8, 0.73, 0.95, 0.48]	40.0	
19	[41.0, -144.0]	[37.0, -144.0]	[3.9, 133.0]	[2.3, 89.0]	[0.96, 0.38, 0.68, 0.37, 0.094]	188.0	
20	[-1.9, -19.0]	[1.1, -12.0]	[0.31, 95.0]	[2.6, 78.0]	[0.12, 0.25, 0.98, 0.33, 0.65]	50.0	

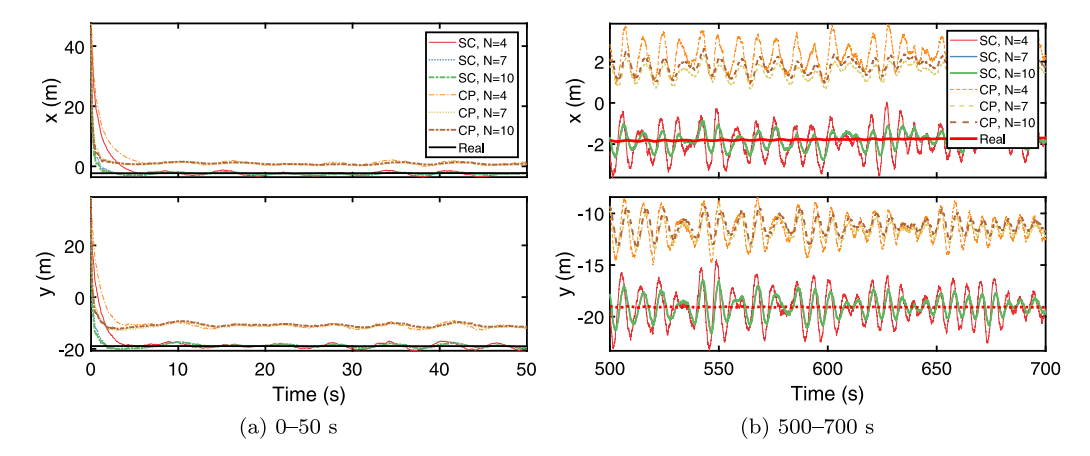


Fig. 8. COT position estimates with various numbers of virtual vessels and current conditions, group (b) and set (III) (SC-with only surface current, CP-with current profile).

bias can be extremely large. Higher n also improves the estimation performance. Therefore, the proposed scheme can be applied to provide additional posref to the position mooring system and estimate the unknown anchor positions.

To enhance the computational speed, we need to find a tradeoff between the speed, time step, and accuracy. A few of the matrices in the EKF have more than 100 rows when n=10, and the matrix operation and its inverses are quite slow to compute. The solution is to program in a language with higher efficiency, in combination with the application of state augmentation and sparsification (Bailey and Durrant-Whyte, 2006).

In addition to the EKF-SLAM approach, we also tried the SOCP and SDP methods. However, we notice that the constraint functions only provide a local optimum, and the results are insufficient to provide accurate localization information. The main reason is the relatively small motion range (the accepted region in Fig. 5) of the upper moored structure.

7. Conclusion and future work

In this paper, a motion estimate for a moored floating structure is achieved by using tension cell measurements equipped on mooring

Z. Ren et al. Ocean Engineering 266 (2022) 112706

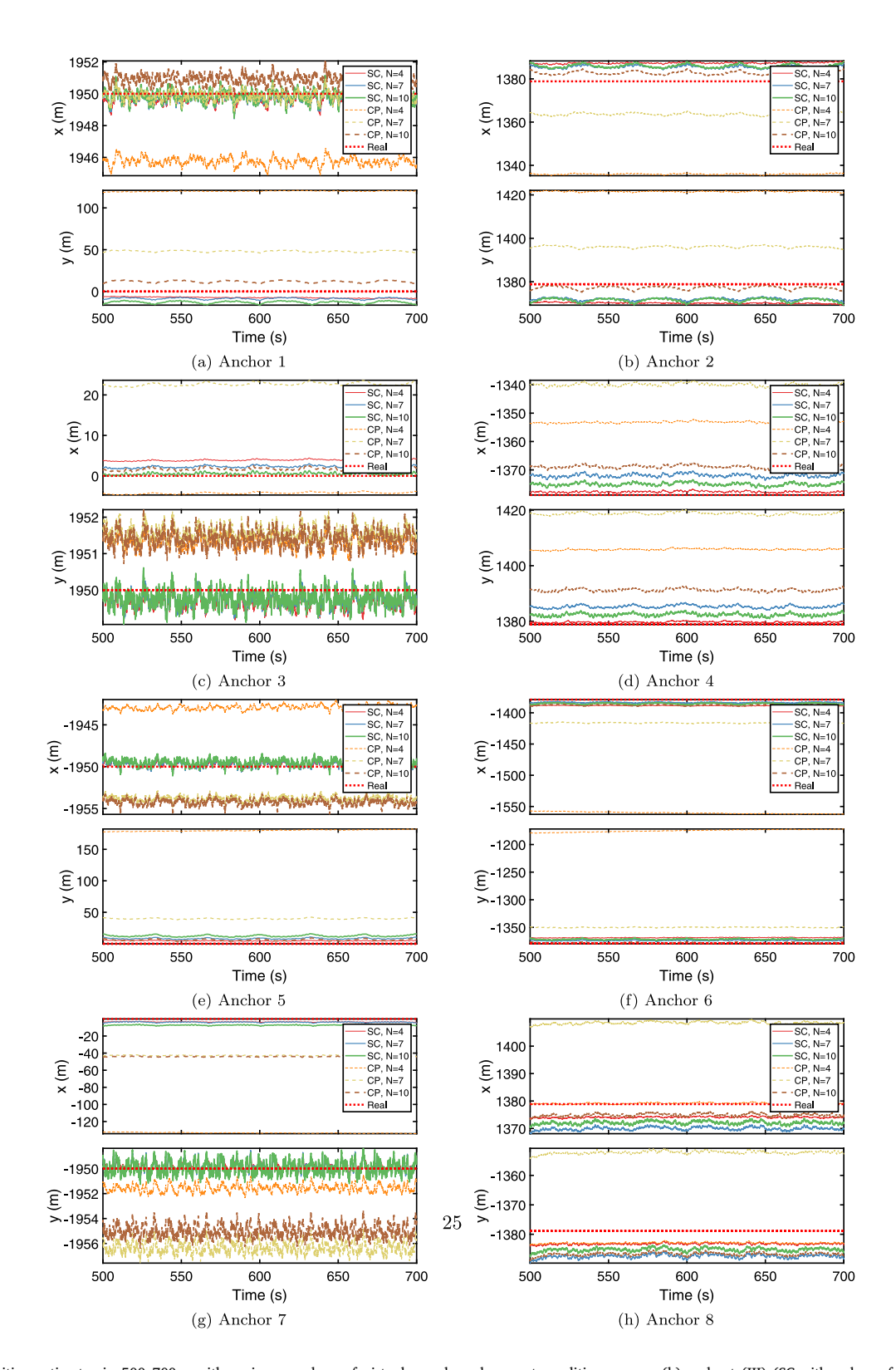


Fig. 9. Anchor position estimates in 500–700 s with various numbers of virtual vessels and current conditions, group (b) and set (III) (SC-with only surface current, CP-with current profile).

lines. Tension measurements are related to range signals with reasonable assumptions and careful discussion. The line-of-sight model contains the influence of the turret.

Range measurement noise and bias are analyzed. A sensor network scheme is built with the previously stored time series. Topological analysis shows that the network should have a number of at least 3

Z. Ren et al. Ocean Engineering 266 (2022) 112706

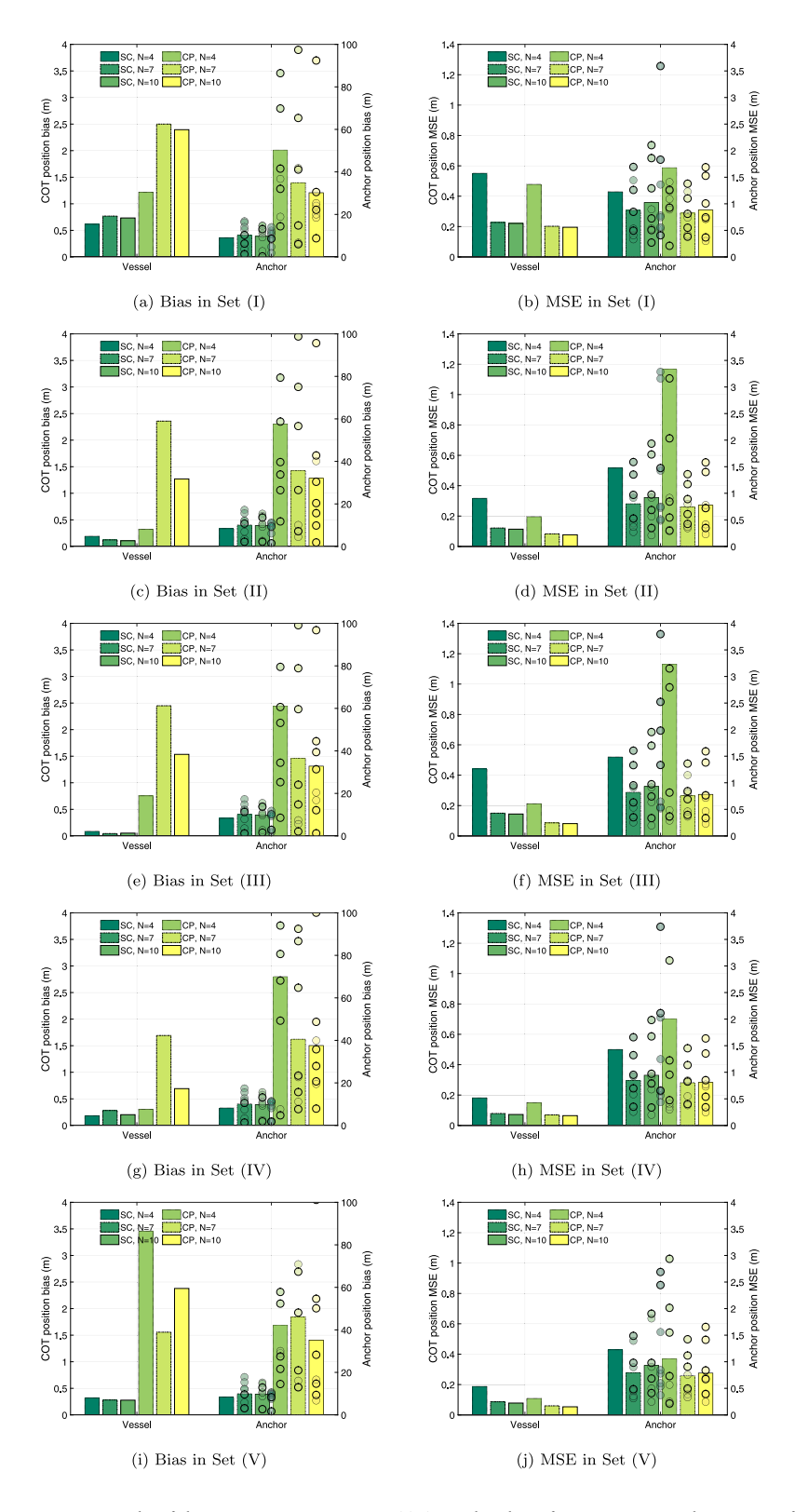


Fig. 10. Statistic results of the position estimates, group (a) (SC-with only surface current, CP-with current profile).

anchors and 3 virtual vessels to maintain the observability. In addition, the observability of the proposed scenario using distributed mooring is improved with an increasing number of virtual vessels and higher proportion of distance between anchors and virtual vessels.

An EKF-based approach is employed to asymptotically estimate the uncertain nodes, and numerical simulations are conducted to verify the proposed algorithm. A comparison study verifies that the technique can well estimate the position of the floating structure COT and anchors.

Z. Ren et al. Ocean Engineering 266 (2022) 112706

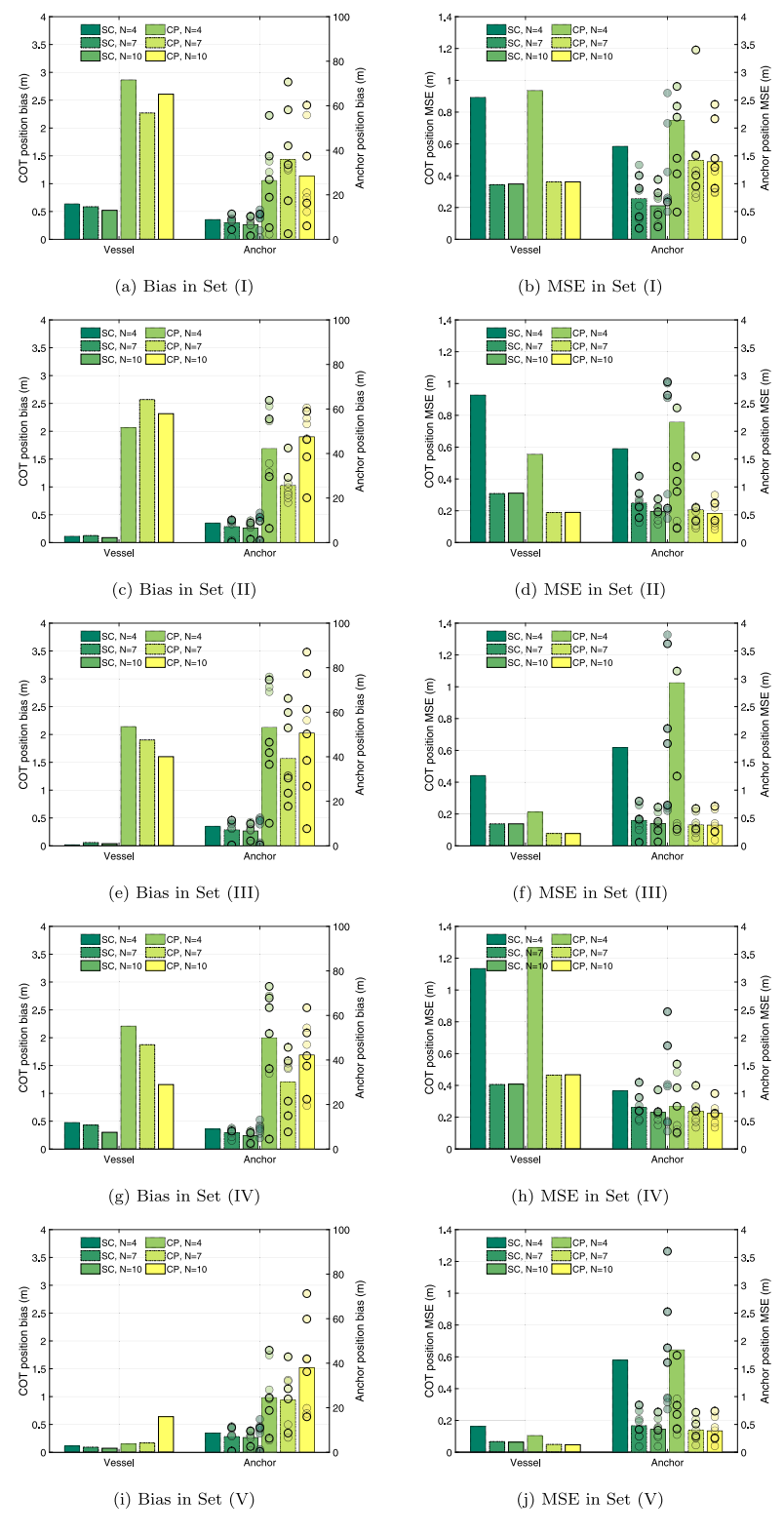


Fig. 11. Statistic results of the position estimates, group (c) (SC-with only surface current, CP-with current profile).

The proposed algorithm not only enhances the system redundancy but also provides a possibility to roughly locate anchors without further investment. However, the loads acting on the mooring lines caused by the underwater current profile influence the estimate accuracy. Therefore, future emphasis will be placed on non-line-of-sight tension measurements to reduce the effects of current profiles and realize more accurate position estimates.

CRediT authorship contribution statement

Zhengru Ren: Conceptualization, Data curation, Methodology, Investigation, Software, Writing – original draft, Funding acquisition. Hongyu Zhou: Conceptualization, Methodology, Investigation, Supervision, Writing – review & editing, Funding acquisition. Binbin Li: Investigation, Writing – review & editing. Zhenzhong Hu: Conceptualization, Methodology, Investigation, Writing – review & editing.

Table 5
List of frequently used symbols and their denotations.

Symbol	Denotation			
i	Index of the anchor			
j	Index of the virtual vessel			
m	Number of anchors			
n	Number of virtual vessels			
$\{A_i\}$	Ancho _i -fixed reference frame			
{ B}	Body-fixed reference frame			
$\{N\}$	NED reference frame			
Ψ	Yaw angle			
x, y, z	Positions in $\{N\}$			
p_r	Real-time horizontal position of the COT			
$p_{fi} = [x_{fi}, y_{fi}]^{T}$	Horizontal position of the fairlead corresponding to Anchor i			
$p_{ai} = [x_{ai}, y_{ai}]^{T}$	Horizontal position of Anchor i			
$p_{tj} = [x_{tj}, y_{tj}]^{T}$	Horizontal position of Virtual vessel j			
$p_p = [x_p, y_p]^{T}$	Real-time LF horizontal position of the COT			
p_a	A vector containing all anchor positions			
p_t	A vector containing all COT positions			
\hat{p}	Estimate of <i>p</i>			
T_i	Tension measurement between Anchor i and real-time COT			
T_{ii}	Tension measurement between Anchor i and Virtual vessel j COT			
T_i^{0}	Noiseless axial tension at the top end of the ith mooring line			
$\Delta T_{i,c}$	Tension deviations due to current loads			
$\Delta T_{i,v}$	Tension deviations due to wave-induced motions			
$\Delta T_{i,s}$	Tension deviations due to seafloor topographical issues			
v_{ti}	Gaussian white noise in tension measurement			
b_{ti}	Sensor bias in tension measurement			
X_i^0	Horizontal distance between the ith anchor and its fairlead			
$d_i, \bar{d_i}$	LOS range measurement and real distance between p_{qi} and p_r			
d_{ii} , \bar{d}_{ii}	LOS range measurement and real distance between p_{ai} and p_{ti}			
d_I	A vector containing all d_i			
$d_{IJ}^{'}$	A vector containing all d_{ij}			
f_i	Tension lookup table by setting heave $z = 0$ without current profile			
k_i, k_{ij}	Generalized stiffness of the mooring line			
c	Underwater current profile			
R	Transformation matrix from $\{B\}$ to $\{N\}$			
r_t	Radius of the COT fairlead circle			
Ψ_t	Turret orientation			

Menghong Yu: Conceptualization, Methodology, Investigation, Writing – review & editing. **Wei Shi:** Investigation, Writing – review & editing, Funding acquisition.

Declaration of competing interest

The authors declare that they have no known competing financial interests or personal relationships that could have appeared to influence the work reported in this paper.

Data availability

Data will be made available on request.

Acknowledgments

This research was supported by the National key research and development program, Ministry of Science and Technology of the People's Republic of China (Grant No. 2022YFC3102603).

References

- Aamo, O.M., Fossen, T.I., 1999. Controlling line tension in thruster assisted mooring systems. In: Control Applications, 1999. Proceedings of the 1999 IEEE International Conference on, vol. 2. IEEE, pp. 1104–1109.
- Aamo, O., Fossen, T., 2001. Finite element modelling of moored vessels. Math. Comput. Model. Dyn. Syst. 7 (1), 47–75.
- Arrichiello, F., Antonelli, G., Aguiar, A.P., Pascoal, A., 2013. An observability metric for underwater vehicle localization using range measurements. Sensors 13 (12), 16191–16215. http://dx.doi.org/10.3390/s131216191.
- Aspnes, J., Eren, T., Goldenberg, D., Morse, A., Whiteley, W., Yang, Y., Anderson, B., Belhumeur, P., 2006. A theory of network localization. IEEE Trans. Mob. Comput. 5 (12), 1663–1678. http://dx.doi.org/10.1109/TMC.2006.174.

- Bailey, T., Durrant-Whyte, H., 2006. Simultaneous localization and mapping (SLAM): Part II. IEEE Robot. Autom. Mag. 13 (3), 108–117.
- Campanile, A., Piscopo, V., Scamardella, A., 2018. Mooring design and selection for floating offshore wind turbines on intermediate and deep water depths. Ocean Eng. 148, 349–360.
- Dai, J., Leira, B.J., Moan, T., Alsos, H.S., 2021. Effect of wave inhomogeneity on fatigue damage of mooring lines of a side-anchored floating bridge. Ocean Eng. 219, 108304.
- Deng, W., Xu, J., Gao, X.-Z., Zhao, H., 2022. An enhanced MSIQDE algorithm with novel multiple strategies for global optimization problems. IEEE Trans. Syst. Man Cybern.: Syst. 52 (3), 1578–1587. http://dx.doi.org/10.1109/TSMC.2020.3030792.Durrant-Whyte, H., Bailey, T., 2006. Simultaneous localization and mapping: part i. Robot. Autom. Mag. IEEE 13 (2), 99–110.
- Fossen, T.I., 2011. Handbook of Marine Craft Hydrodynamics and Motion Control. John Wiley & Sons.
- Fossen, T.I., Strand, J.P., 1999. Passive nonlinear observer design for ships using Lyapunov methods: full-scale experiments with a supply vessel. Automatica 35 (1), 3–16.
- Guo, X., Zhang, X., Tian, X., Lu, W., Li, X., 2022. Probabilistic prediction of the heave motions of a semi-submersible by a deep learning model. Ocean Eng. 247, 110578.
 Gustafsson, F., 2010. Statistical Sensor Fusion. Studentlitterat, Lund, Sweden.
- Ja'e, I.A., Osman Ahmed Ali, M., Yenduri, A., Nizamani, Z., Nakayama, A., 2022. Optimisation of mooring line parameters for offshore floating structures: A review paper. Ocean Eng. 247, 110644.
- Ji, S., Choi, M., Kim, Y., 2015. A study on position mooring system design for the vessel moored by mooring lines. Mechatron. IEEE/ASME Trans. PP (99), 1–8. http://dx.doi.org/10.1109/TMECH.2015.2407612.
- Lee, K., Chung, M., Kim, S., Shin, D.H., 2021. Damage detection of catenary mooring line based on recurrent neural networks. Ocean Eng. 227, 108898.
- Li, L., Jiang, Z., Ong, M.C., Hu, W., 2019. Design optimization of mooring system: an application to a vessel-shaped offshore fish farm. Eng. Struct. 197, 109363.
- Lui, K.W.-K., Ma, W.-K., So, H.-C., Chan, F.K., 2009. Semi-definite programming algorithms for sensor network node localization with uncertainties in anchor positions and/or propagation speed. IEEE Trans. Signal Process. 57 (2), 752–763.
- May, P., Sanderson, D., Sharp, J., Stacey, A., 2008. Structural integrity monitoring: Review and appraisal of current technologies for offshore applications. In: ASME 2008 27th International Conference on Offshore Mechanics and Arctic Engineering. American Society of Mechanical Engineers, pp. 247–263.

- MSS. Marine Systems Simulator, 2010. Viewed 30.10.2014. URL http://www.marinecontrol.org.
- Naddafzadeh-Shirazi, G., Shenouda, M.B., Lampe, L., 2014. Second order cone programming for sensor network localization with anchor position uncertainty. Wirel. Commun. IEEE Trans. 13 (2), 749–763.
- Nguyen, D.H., Nguyen, D.T., Quek, S.T., Sørensen, A.J., 2011. Position-moored drilling vessel in level ice by control of riser end angles. Cold Reg. Sci. & Technol. 66 (2-3), 65-74.
- Nord, 2011. Loss of anchors and chain. URL http://www.gard.no/ikbViewer/web/ updates/content/11831736/loss-of-anchors-and-chain.
- Peng, Z., Zhao, H., Li, X., 2021. New ductile fracture model for fracture prediction ranging from negative to high stress triaxiality. Int. J. Plast. 145, 103057. http: //dx.doi.org/10.1016/j.ijplas.2021.103057.
- Ratcovich, M., 2008. The nairobi international convention on the removal of wrecks in light of existing marine liability regimes.
- Ren, Z., Han, X., Yu, X., Skjetne, R., Leira, B.J., Sævik, S., Zhu, M., 2023. Data-driven simultaneous identification of the 6DOF dynamic model and wave load for a ship in waves. Mech. Syst. Signal Process. 184. 109422.
- Ren, Z., Jiang, Z., Skjetne, R., Gao, Z., 2018. Development and application of a simulator for offshore wind turbine blades installation. Ocean Eng. 166, 380-395.
- Ren, Z., Skjetne, R., 2016a. An on-site current profile estimation algorithm for a moored floating structure. IFAC-PapersOnLine 49 (23), 153–158.
- Ren, Z., Skjetne, R., 2016b. A tension-based position estimation solution of a moored structure and its uncertain anchor positions. IFAC-PapersOnLine 49 (23), 251–257.
- Ren, Z., Skjetne, R., Jiang, Z., Gao, Z., Verma, A.S., 2019. Integrated GNSS/IMU hub motion estimator for offshore wind turbine blade installation. Mech. Syst. Signal Process. 123, 222–243.

- Ren, Z., Skjetne, R., Kjerstad, Ø.K., 2015. A tension-based position estimation approach for moored marine vessels. IFAC-PapersOnLine 48 (16), 248–253.
- Shi, W., Zhang, L., Karimirad, M., Michailides, C., Jiang, Z., Li, X., 2023. Combined effects of aerodynamic and second-order hydrodynamic loads for three semisubmersible floating wind turbines in different water depths. Appl. Ocean Res. 130, 103416
- Skjetne, R., Ren, Z., 2020. A survey on modeling and control of thruster-assisted position mooring systems. Mar. Struct. 74, 102830.
- Tseng, P., 2007. Second-order cone programming relaxation of sensor network localization. SIAM J. Optim. 18 (1), 156–185.
- Williams, R.K., Sukhatme, G.S., 2015. Observability in topology-constrained multirobot target tracking. In: 2015 IEEE International Conference on Robotics and Automation. pp. 1795–1801. http://dx.doi.org/10.1109/ICRA.2015.7139431.
- Wu, B., 2022. Synthesis of Human-in-the-Loop Navigational Operations towards Maritime Autonomous Surface Ships (Ph.D. thesis). Norwegian University of Science and Technology.
- Zeng, Y., Shi, W., Michailides, C., Ren, Z., Li, X., 2022. Turbulence model effects on the hydrodynamic response of an oscillating water column (OWC) with use of a computational fluid dynamics model. Energy 261, 124926. http://dx.doi.org/10. 1016/j.energy.2022.124926.
- Zhang, Y., Shi, W., Li, D., Li, X., Duan, Y., Verma, A.S., 2022. A novel framework for modeling floating offshore wind turbines based on the vector form intrinsic finite element (VFIFE) method. Ocean Eng. 262, 112221.
- Zhen, X., Vinnem, J.E., Peng, C., Huang, Y., 2018. Quantitative risk modelling of maintenance work on major offshore process equipment. J. Loss Prev. Process Ind. 56, 430–443.
- Zhou, L., Gao, J., Xu, S., Bai, X., 2018. A numerical method to simulate ice drift reversal for moored ships in level ice. Cold Reg. Sci. & Technol. 152, 35–47.